5-22-2013

Coevolution of Nonlinear trends in Vegetation, Soils, and Topography with Elevation and Slope Aspect: A Case Study in the Sky Islands of Southern Arizona

Jon D. Pelletier
University of Arizona

Greg A. Barron-Gafford
University of Arizona

David D. Breshears
University of Arizona

Paul D. Brooks
University of Arizona

Jon Chorover
University of Arizona

See next page for additional authors

Recommended Citation

Pelletier, J. D., G. A. Barron-Gafford, D. D. Breshears, P. D. Brooks, J. Chorover, M. Durcik, C. J. Harman, T. E. Huxman, K. A. Lohse, R. Lybrand, T. Meixner, J. C. McIntosh, S. A. Papuga, C. Rasmussen, M. Schaap, T. L. Swetnam, and P. A. Troch (2013), Coevolution of nonlinear trends in vegetation, soils, and topography with elevation and slope aspect: A case study in the sky islands of southern Arizona, *J. Geophys. Res. Earth Surf.*, *118*, 741–758, doi:10.1002/jgrf.20046.

JOURNAL OF GEOPHYSICAL RESEARCH: EARTH SURFACE, VOL. 118, 741–758, doi:10.1002/jgrf.20046, 2013

Coevolution of nonlinear trends in vegetation, soils, and topography with elevation and slope aspect: A case study in the sky islands of southern Arizona

Jon D. Pelletier,[1] Greg A. Barron-Gafford,[2,3] David D. Breshears,[3,4] Paul D. Brooks,[5] Jon Chorover,[6] Matej Durcik,[5] Ciaran J. Harman,[5] Travis E. Huxman,[2,3] Kathleen A. Lohse,[4,7] Rebecca Lybrand,[6] Tom Meixner,[5] Jennifer C. McIntosh,[5] Shirley A. Papuga,[4] Craig Rasmussen,[6] Marcel Schaap,[6] Tyson L. Swetnam,[4] and Peter A. Troch[5]

Received 24 July 2012; revised 8 February 2013; accepted 11 February 2013; published 22 May 2013.

[1] Feedbacks among vegetation dynamics, pedogenesis, and topographic development affect the "critical zone"—the living filter for Earth's hydrologic, biogeochemical, and rock/sediment cycles. Assessing the importance of such feedbacks, which may be particularly pronounced in water-limited systems, remains a fundamental interdisciplinary challenge. The sky islands of southern Arizona offer an unusually well-defined natural experiment involving such feedbacks because mean annual precipitation varies by a factor of five over distances of approximately 10 km in areas of similar rock type (granite) and tectonic history. Here we compile high-resolution, spatially distributed data for Effective Energy and Mass Transfer (EEMT: the energy available to drive bedrock weathering), above-ground biomass, soil thickness, hillslope-scale topographic relief, and drainage density in two such mountain ranges (Santa Catalina: SCM; Pinaleño: PM). Strong correlations exist among vegetation-soil-topography variables, which vary nonlinearly with elevation, such that warm, dry, low-elevation portions of these ranges are characterized by relatively low above-ground biomass, thin soils, minimal soil organic matter, steep slopes, and high drainage densities; conversely, cooler, wetter, higher elevations have systematically higher biomass, thicker organic-rich soils, gentler slopes, and lower drainage densities. To test if eco-pedo-geomorphic feedbacks drive this pattern, we developed a landscape evolution model that couples pedogenesis and topographic development over geologic time scales, with rates explicitly dependent on vegetation density. The model self-organizes into states similar to those observed in SCM and PM. Our results highlight the potential importance of eco-pedo-geomorphic feedbacks, mediated by soil thickness, in water-limited systems.

Citation: Pelletier, J. D., G. A. Barron-Gafford, D. D. Breshears, P. D. Brooks, J. Chorover, M. Durcik, C. J. Harman, T. E. Huxman, K. A. Lohse, R. Lybrand, T. Meixner, J. C. McIntosh, S. A. Papuga, C. Rasmussen, M. Schaap, T. L. Swetnam, and P. A. Troch (2013), Coevolution of nonlinear trends in vegetation, soils, and topography with elevation and slope aspect: A case study in the sky islands of southern Arizona, *J. Geophys. Res. Earth Surf.*, *118*, 741–758, doi:10.1002/jgrf.20046.

[1]Department of Geosciences, University of Arizona, Tucson, Arizona, USA.
[2]Department of Ecology and Evolutionary Biology, University of Arizona, Tucson, Arizona, USA.
[3]Biosphere 2, University of Arizona, Tucson, Arizona, USA.
[4]School of Natural Resources and the Environment, University of Arizona, Tucson, Arizona, USA.
[5]Department of Hydrology and Water Resources, University of Arizona, Tucson, Arizona, USA.
[6]Department of Soil, Water, and Environmental Sciences, University of Arizona, Tucson, Arizona, USA.
[7]Department of Biological Sciences, Idaho State University, Pocatello, Idaho, USA.

Corresponding author: J. D. Pelletier, Department of Geosciences, University of Arizona, Tucson, AZ 85721, USA. (jdpellet@email.arizona.edu)

2169-9003/13/10.1002/jgrf.20046

1. Introduction

[2] Upland landscapes, i.e., those in which soil (if present) overlies bedrock, develop in response to the local history of tectonics and climate over time scales of thousands to millions of years. Limitations in our understanding of how climate influences topography stems, in part, from the existence of complex feedback relationships among vegetation dynamics, pedogenesis, and topographic development. For example, climate influences the vegetation cover that a given landscape can support. More vegetation, in turn, leads to higher colluvial sediment fluxes via an increase in bioturbation [e.g., *Walther et al.*, 2009]. All else being equal, higher colluvial sediment fluxes lead, over time, to thinner soils. A more humid climate, however, also tends to enhance rates of

soil production from bedrock, potentially resulting in thicker soils. Soil thickness, in turn, influences how much biomass a given hillslope can support in water-limited environments since thinner soils store less water. Addressing these complex feedback relationships is central to the challenge of understanding the "critical zone"—the living filter for Earth's hydrologic, biogeochemical, and rock/sediment cycles [e.g., *Chorover et al*., 2011]. Quantifying these and other feedback mechanisms among vegetation dynamics, pedogenesis, and topographic development requires models that incorporate the effects of vegetation density and soil thickness explicitly in the differential equations that describe topographic development. Some excellent initial modeling studies have illustrated how vegetation cover can affect rates of slope-wash and fluvial erosion and hence drainage density [e.g., *Istanbulluoglu and Bras*, 2005]. However, vegetation also influences regolith production and colluvial transport rates in ways that have not yet been integrated into landscape evolution models. In this paper, we present a preliminary model for the eco-pedo-geomorphic evolution of water-limited landscapes of southern Arizona as a first step towards developing a comprehensive model for the long-term coevolution of vegetation, soils, and topography in upland landscapes generally.

2. Site Description and Prior Work

[3] Southern Arizona is home to two mountain ranges, the Santa Catalina (SCM) and Pinaleño Mountains (PM), that are ideal locations to study the coevolution of vegetation, soils, and topography over geologic timescales (Figure 1). The term "sky islands" refers to the forested areas at high elevations surrounded by the "seas" of desert-scrub-dominated communities at lower elevations. Both ranges are primarily granitic in composition, and both have undergone a similar history of extensional tectonics from the Oligocene to the Miocene [*Spencer and Reynolds*, 1989; *Dickinson*, 1991; *Davis et al*., 2004]. These ranges are relatively mature; i.e., for at least the past 10 million years, they have not been subject to active tectonic uplift. As such, they are in a state of topographic decline with uplift occurring by flexural-isostatic rebound [*Pelletier*, 2010a]. Mean annual precipitation in the sky islands varies by approximately a factor of five (from approximately 0.2 m yr^{-1} at approximately 1 km elevation above sea level (asl) to 1 m yr^{-1} at 2.5–3.0 km asl) over a horizontal distance of only 10 km.

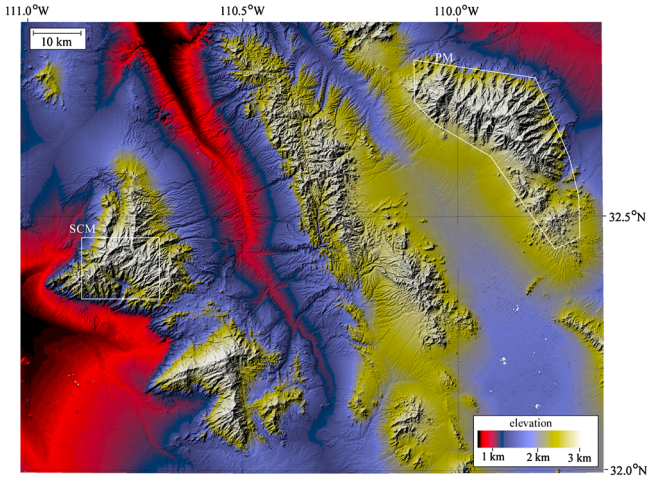

Figure 1. Shaded-relief image of the study region in southern Arizona, including Santa Catalina Mountains (SCM) and Pinaleño Mountains (PM). The approximate extent of airborne lidar coverage is shown in white polygons.

[4] The elevation/climate gradients of the southern Arizona sky islands have figured prominently in the history of ecology [*McIntosh*, 1986]. *Merriam* [1890], for example, was the first to document (using the sky islands of Arizona as type examples) that the elevational zonation of vegetation was a response of species and communities to covarying temperature and precipitation gradients [*Briggs and Humphries*, 2004]. Subsequently, *Whittaker and Niering* [1975] quantified biomass, productivity, and species diversity across the climate/elevation gradient of SCM. Perhaps the preeminent plant ecologist of the late twentieth century [*Brown and Sax*, 2004], Whittaker recognized the unusually well-defined natural experiment posed by the southern Arizona sky islands and devoted much of his career to studying the climatic control of vegetation in SCM. A key goal of this paper is to utilize the elevation/climate gradient of the sky islands to establish trends in soil and topographic measures, and their inter-dependences, analogous to the trends documented by *Whittaker and Niering* [1975] for vegetation density. We consider both SCM and PM in this study to ensure that the patterns we observe are robust across multiple ranges. It should be noted that we chose to limit the analysis of SCM to only the granitic core of the range since the southern forerange is comprised of banded gneiss [e.g., *Dickinson*, 1991].

[5] SCM has been the subject of one other study aimed at quantifying the climatic control of topography. *Etheredge et al*. [2004] compared the drainage density in SCM to that of the Hualapai Mountains located in northwest Arizona approximately 500 km away. The Hualapai Mountains have a lower drainage density, a result that *Etheredge et al*. [2004] concluded was the result of more summertime rainfall in SCM compared to the Hualapai Mountains, given that both ranges have otherwise similar mean annual precipitation, dominant rock type, and tectonic history. While *Etheredge et al*. [2004] emphasized the differences in topography between ranges, the focus of this paper is on the substantial variability within ranges along the elevation/climate gradient.

3. Empirical Analysis

3.1. Summary

[6] Before we document the methods used to quantify trends in landscape variables across the elevation/climate gradient, it is helpful to summarize the results of our empirical work so that the big-picture relationships among vegetation, soil, and topography across the climate/elevation gradient are clear. Trends in vegetation, soils, and geomorphology are nonlinear across the elevation/climate gradients of SCM and PM (Figure 2). Although there are some differences between the two ranges (documented in detail later in this section), both ranges show consistent variations across the elevation/climate gradient in Effective Energy and Mass Transfer (EEMT), above-ground (live dry) biomass (AGB), soil thickness, hillslope-scale relief, and mean

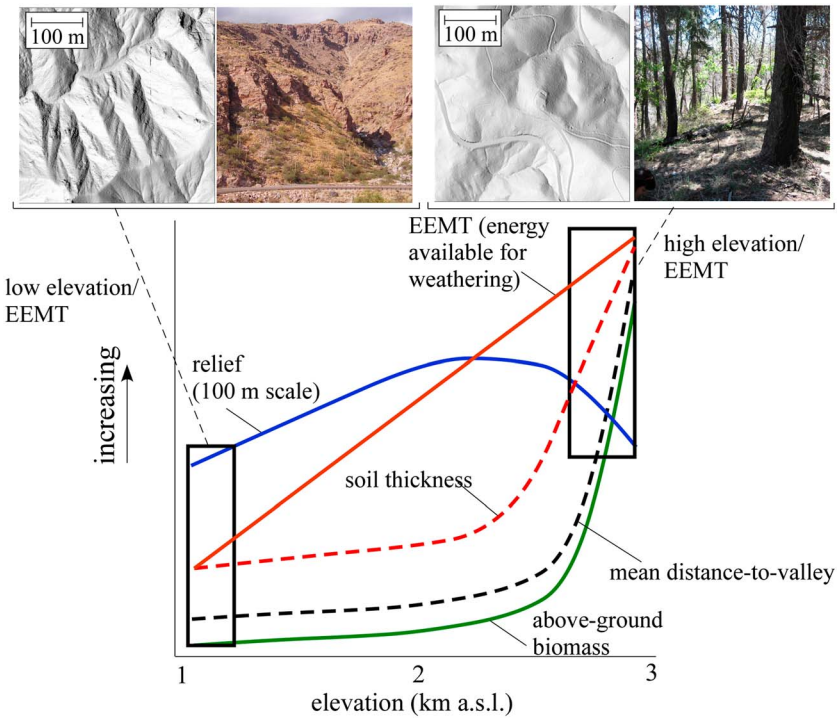

Figure 2. Schematic illustration of trends in EEMT, above-ground biomass (AGB), soil thickness, mean distance-to-valley, and relief as functions of elevation in SCM and PM with variable units but consistently linear *Y* axis scales based on empirical data presented in more detail in Figures 3–7. EEMT increases approximately linearly with elevation. Above-ground biomass, soil thickness, and mean distance-to-valley increase nonlinearly with elevation. Relief is relatively unchanged, increasing moderately before reaching a maximum and then declining at highest elevation. Representative landscapes are shown at top using field photographs and shaded-relief images of airborne-lidar DEMs.

distance-to-valley (the latter being inversely related to drainage density [*Tucker et al*., 2001]). EEMT is a variable that combines precipitation and temperature into a single energy-based variable that *Rasmussen et al*. [2005] and *Pelletier and Rasmussen* [2009a] showed correlates well with rates of bedrock weathering, particularly for granitic rocks in semi-arid environments such as SCM and PM. Hillslope-scale relief in this paper refers to the maximum difference in elevation between two points separated by at most 100 m. Mean distance-to-valley is the average distance along the path of steepest descent between each point and the nearest valley bottom where a zone of concentrated water flow occurs (as opposed to sheet flow or rill flow, which are dominant on hillslopes or in hollows). Mean distance-to-valley is important hydrologically because it controls hydrologic partitioning; i.e., if mean distance-to-valley is large, hillslopes are relatively long (~100 m or more) and more precipitation that falls on the landscape has a chance to infiltrate into soil before it reaches the valley network. Conversely, if mean distance-to-valley is small, hillslopes are relatively short (~10 m) and more water that falls on the landscape tends to reach the valley bottoms where it can be routed off the landscape more rapidly. Mean distance-to-valley is important geomorphically because it is a measure of the relative importance of colluvial and fluvial process rates, with areas of lower mean distance-to-valley characterized by a lower ratio of colluvial to fluvial erosion rates [*Tucker and Bras*, 1998; *Perron et al*., 2008].

[7] At low elevations in SCM and PM, EEMT is low (0–10 MJ m^{-2} yr^{-1}), above-ground biomass (AGB) estimated from airborne-lidar data is low (~1–10 kg m^{-2}; i.e., approximately 1 to 1.5 orders of magnitude lower than in the high-elevation forest), mean distance-to-valley is low (~10 m), soils are thin (10–30 cm), and relief is moderate (approximately 20 m/100 m) (Figure 2). At high elevations, EEMT is high (30–45 MJ m^{-2} yr^{-1}), above-ground biomass is high (~10–100 kg/m^2), mean distance to valley is high (~100 m), soils are thick (0.7–1.0 m), and relief is moderate (20 m/100 m). Across the gradient, above-ground biomass, mean distance-to-valley, and soil thickness increase rapidly and nonlinearly with increasing elevation. Relief shows a more complex pattern, increasing modestly and then decreasing with increasing elevation. The photos and shaded-relief images in Figure 2 illustrate these differences visually. The upper right-most images show an example of a well-rounded and heavily vegetated (i.e., a Ponderosa Pine (*Pinus ponderosa*) or mixed-conifer forest) hillslope drainage divide characteristic of high elevation areas in SCM and PM. At high elevations, topography tends to be of the ridge-and-ravine type with relatively low drainage density, thick soils, and few bedrock outcrops. At lower elevations (upper left-most images), hillslopes are generally shorter; there is a preponderance of desert scrub vegetation with biomass dominated by Saguaro cacti (*Carnegiea gigantean*) and Palo Verde trees (*Cercidium microphyllum*). Hillslopes with vertical-walled cliffs (separated by more gently sloping hillslope segments) and abundant

natural bedrock outcrops are common. In this section, we document the trends in vegetation, soils, and topography as a function of elevation and slope aspect in SCM and PM using historical climate data, airborne-lidar data, and field measurements. In section 4, we present a numerical model that reproduces the first-order patterns in the data and that illustrates the important role of feedback relationships among vegetation dynamics, pedogenesis, and topographic development in generating these patterns.

3.2. Effective Energy and Mass Transfer (EEMT)

[8] The energy available to drive bedrock weathering is a function of water availability (since water acts as a catalyst in many if not all weathering mechanisms), the temperature of the available water, and primary production (which acts to break down rock, e.g., via the mechanical action of roots, the infusion of reduced carbon, etc.). In this study, we use EEMT to quantify the rate of bedrock breakdown into soil. The rate of bedrock breakdown into soil is fundamental to the coevolution of vegetation, soils, and topography because it controls the rate at which soil accumulates on slopes, which in turn controls how much vegetation can be supported on the hillslope, and the colluvial sediment flux. Theoretical arguments based on nonequilibrium thermodynamics suggest that EEMT is an optimal, climatically based variable for quantitative prediction of weathering rates. The climatic dependence of rock-weathering rates has been shown to be more effectively predicted by EEMT than by other individual climatic and/or resulting biotic parameters such as mean annual temperature, mean annual precipitation, or net primary production [*Rasmussen et al*., 2011].

[9] The steps required to calculate EEMT from an input DEM and climate data have been discussed elsewhere [i.e., *Chorover et al*., 2011]; hence, we outline the steps only briefly here. EEMT is the sum of energy input via effective precipitation (precipitation in excess of evapotranspiration), E_{PPT}, and net primary production, E_{BIO}, where

$$E_{\mathrm{PPT}} = \Delta T \cdot C_{\mathrm{W}} \cdot P_{\mathrm{eff}}, \tag{1}$$

$$E_{BIO} = NPP \cdot h_{\mathrm{BIO}}, \tag{2}$$

[10] NPP is net ecosystem production of biomass, h_{BIO} is specific biomass energy content $[22 \times 10^6\,\mathrm{J\,kg^{-1}}]$, $\Delta T = T_{\mathrm{ambient\ air}} - 273°\mathrm{K}$, C_{w} is the specific heat of water $[\mathrm{J\,kg^{-1}\,K^{-1}}]$, and P_{eff} (net precipitation) $= PPT - ET$ $[\mathrm{kg\,m^{-2}\,s^{-1}}]$. However, because NPP and ET are not easily mapped in some locations due to limited data, *Chorover et al*. [2011] developed a multiple linear regression model for EEMT based solely on locally modified temperature, T (°C) (modified to account for microclimatic effects due to topography), mean annual precipitation, P (cm), and vapor pressure deficit, VPD (Pa), i.e., variables that are quantifiable for most locations on Earth using readily available input DEM and climate data. This regression combines T, P, and VPD in a way that closely mimics variations in $E_{\mathrm{PPT}} + E_{\mathrm{BIO}}$.

[11] EEMT must be calculated on a sub-annual (e.g., monthly) basis in order to capture the effects of seasonality in climatic variables. The EEMT calculations in this paper were made using data from the PRISM Climate Group at Oregon State University (http://www.prismclimate.org). Climate data are provided at an 800 m spatial resolution for input precipitation, minimum and maximum temperature, and at 4000 m spatial resolution for dew point temperature [*Daly et al*., 2002]. However, PRISM climate data do not account for localized variations in EEMT that result from smaller spatial scale changes in hillslope gradient and aspect as occurs within catchments. To address this issue, these data were then combined with 10 m digital elevation maps (DEM) in order to compute the effects of local slope and aspect on incoming solar radiation and hence locally modified temperature [Yang et al., 2007]. Monthly average dew point temperatures were computed using 10 years of monthly data (2000–2009) and converted to vapor pressure. Precipitation, temperature, and dew point data were re-sampled to 10 m grid using spline interpolation. Monthly solar radiation data (direct and diffuse) were computed using ArcGIS Solar Analyst extension and 10 m elevation data (USGS National Elevation Dataset (NED) 1/3 Arc Second downloaded from the National Map Seamless Server at http://seamless.usgs.gov/). Locally modified temperature was used to compute saturated vapor pressure, and local VPD was estimated as the difference between saturated and actual vapor pressure. The regression model was derived using the ISOHYS climate dataset comprised of approximately 30 year average monthly means for over 300 weather stations spanning all latitude and longitude [*IAEA*, 2004; *Rasmussen and Tabor*, 2007]. The best fit regression model for monthly EEMT is

$$\begin{aligned} EEMT_m = {} & -3.13 + 0.00879(T + 273.15) \\ & + 0.562P + 0.0326\,(T - 17.65)\,(P - 9.0) \\ & - 0.00235VPD + 0.00062\,(P - 9.0)\,(VPD - 662) \end{aligned} \tag{3}$$

[12] Yearly EEMT (in MJ $\mathrm{m^{-2}\ yr^{-1}}$) was calculated by summing over the 12 monthly values.

[13] Elevation is a dominant influence on EEMT in SCM and PM, with EEMT increasing from nearly zero to 35 MJ $\mathrm{m^{-2}\ yr^{-1}}$ for SCM and 45 MJ $\mathrm{m^{-2}\ yr^{-1}}$ for PM (Figure 3). Trends of mean EEMT versus elevation for north- and south-facing slopes within each range (Figure 3a) were computed by averaging the data in the maps in Figures 3b and 3c using 100 m elevation bins. The trend of EEMT for the north-facing slopes of SCM (PM) is labeled as SCM-N (PM-N), and the trend for the south-facing slopes is labeled as SCM-S (PM-S). PM exhibits slightly lower EEMT values for similar elevations compared to SCM, a result likely due to the fact that PM is located farther from the dominant summer moisture source (the Gulf of California). Mean annual rainfall for SCM ranges from 0.33 to 0.95 m $\mathrm{yr^{-1}}$ according to the PRISM data of *Daly et al*. [2002]. PM has a similar range (0.37 to 0.98 m $\mathrm{yr^{-1}}$), but the elevations at which similar values occur are shifted upward by approximately 300–400 m in elevation higher than those of SCM. At intermediate elevations (i.e., 1.5–2.3 km asl), an average difference of approximately 10 MJ $\mathrm{m^{-2}\ yr^{-1}}$ exists between north- and south-facing slopes or approximately 25% of the maximum EEMT for each range. Aspect control is apparent in the map images of Figures 3b and 3c, with north-facing slopes having higher EEMT compared to south-facing slopes due to their reduced radiant forcing and hence greater moisture availability. EEMT does not vary as significantly with slope aspect at low elevations because EEMT values

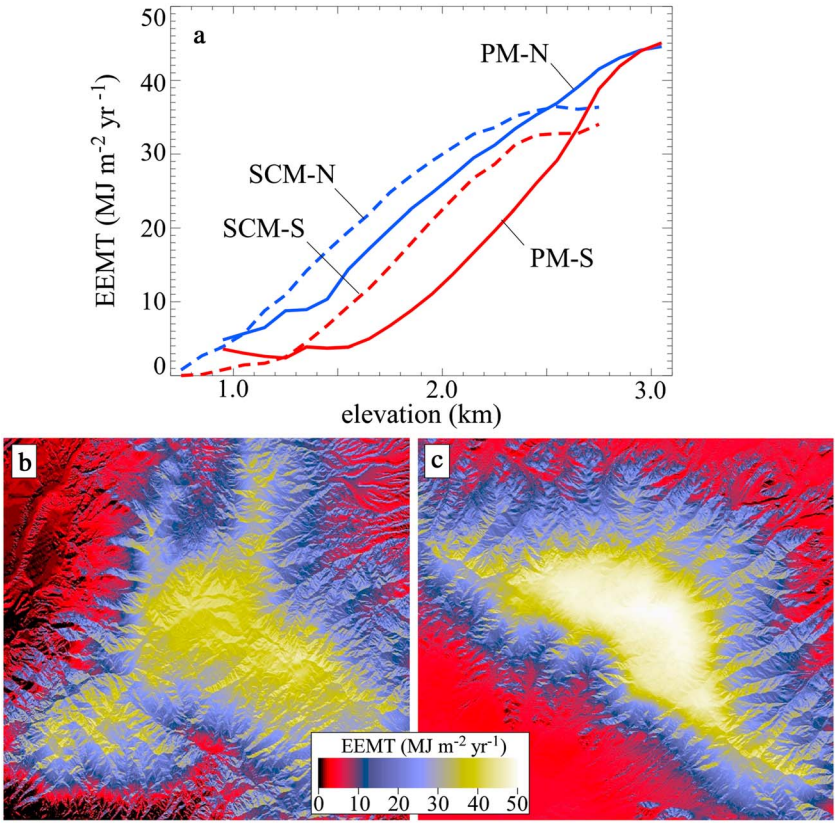

Figure 3. (a) Plots of mean EEMT versus elevation for north- (blue curves) and south-facing (red curves) slopes in SCM (dashed curves) and PM (solid curves). Color maps of EEMT in (b) SCM and (c) PM. The trend of EEMT for the north-facing slopes of SCM (PM) is labeled as SCM-N (PM-N), and the trend for the south-facing slopes is labeled as SCM-S (PM-S). Similar labels are used in Figures 4–6.

there are low to begin with. EEMT also varies minimally with slope aspect at high elevations also because slopes at high elevations are less steep, on average, compared to intermediate elevations.

3.3. Above-Ground Biomass

[14] Above-ground (live dry) biomass (AGB) and its variation with EEMT are important to quantify because vegetation cover controls rates of colluvial transport (i.e., more vegetation cover drives greater bioturbation) and fluvial transport (i.e., more vegetation cover increases the shear stress necessary to erode sediment beneath the canopy, thereby decreasing slope-wash/fluvial erosion rates for conditions of similar runoff). AGB is just one measure of vegetation cover that likely controls sediment transport rates. Sediment transport could be as closely or more closely related to net primary productivity, leaf area index, below-ground biomass, or the rates of change in these quantities over time. Nevertheless, it is reasonable to use AGB as a characteristic variable for quantifying the effect of vegetation cover on geomorphic transport rates because AGB is the most direct measure of how much vegetation is on the landscape and because many vegetation parameters correlate closely with each other in any case (e.g., AGB and below-ground biomass are highly correlated in SCM [e.g., *Whittaker and Niering*, 1975]).

[15] AGB was mapped in SCM and PM using a power-law regression with airborne-lidar-derived mean canopy height (MCH) following *Asner et al.* [2012], i.e.,

$$AGB = a{\cdot}MCH^{b} \tag{4}$$

[16] When applying equation (4), parameters a and b are first calibrated for the study site using lidar-derived MCH and field-surveyed AGB (in plots where biomass has been measured for individual trees and then aggregated to obtain the AGB of the plot). Then, equation (4) is used to estimate AGB across the study site using lidar-derived MCH at 10 m resolution. In this study, we used field-measured biomass data from 79 U.S. Forest Service plots in SCM to calibrate equation (4). We then applied equation (4) to estimate the biomass in all areas of airborne lidar coverage in both SCM and PM. In previous studies [e.g., *Asner et al.*, 2012], the exponents in equation (4) have generally been found to be in the range of 1 to 2. Our regression yielded $a = 0.075$ kg m$^{-4.1}$ and $b = 2.1$. These values were used to map AGB at a 10 m resolution for each range, and these data were then averaged in 100 m wide elevation bins, with north- and south-facing slopes considered separately. Our estimates for AGB at the lowest elevations of each range, which are dominated by desert scrub vegetation, are gross approximations since they are based on a regression equation from the high-elevation forest of SCM. Nevertheless, our estimates

for AGB at low elevations are comparable to those of *Whittaker and Niering* [1975].

[17] Average AGB increases nonlinearly with elevation in both ranges from a low of a few kg m^{-2} to a maximum of approximately 60 kg m^{-2} in SCM and 75 kg m^{-2} in PM (Figure 4). An exponential relationship captures the increase in AGB with EEMT when the data from Figures 3 and 4 are combined, i.e.,

$$AGB = \varepsilon \exp(f \cdot EEMT) \tag{5}$$

with $\varepsilon \approx 1$ kg m^{-2} and $f \approx 0.1$ yr m^2 MJ^{-1}. These values do not represent the relationship between AGB and EEMT in either range precisely but rather represent an average of the trends from the two ranges that is useful for relating AGB to EEMT in the numerical model presented in section 4. At similar elevations, AGB is significantly lower in PM compared to SCM, a result consistent with the lower MAP (and hence EEMT) in PM compared to SCM. AGB decreases in the highest elevations of both ranges, a result attributable to historic wildfires (e.g., AGB maps in Figures 4b and 4c show areas of unusually low biomass in the locations of recent large wildfires). A century of fire suppression has led to unusually large recent fires at the highest elevations of both ranges where fuels have been able to accumulate in large, spatially connected domains. Historic wildfires have been less common at lower elevations in both ranges because fuel loads are naturally more spatially discontinuous at these elevations. AGB increases significantly with increasing elevation starting at 1.5 km asl in SCM and 2.0 km asl in PM (at EEMT values of c. 20 MJ m^{-2} yr^{-1}). Both ranges have significantly more AGB on north-facing slopes compared to south-facing slopes, with the greatest aspect difference occurring in PM, where north-facing slopes at 2.5 km elevation have more than twice the AGB as south-facing slopes. The results in Figure 4

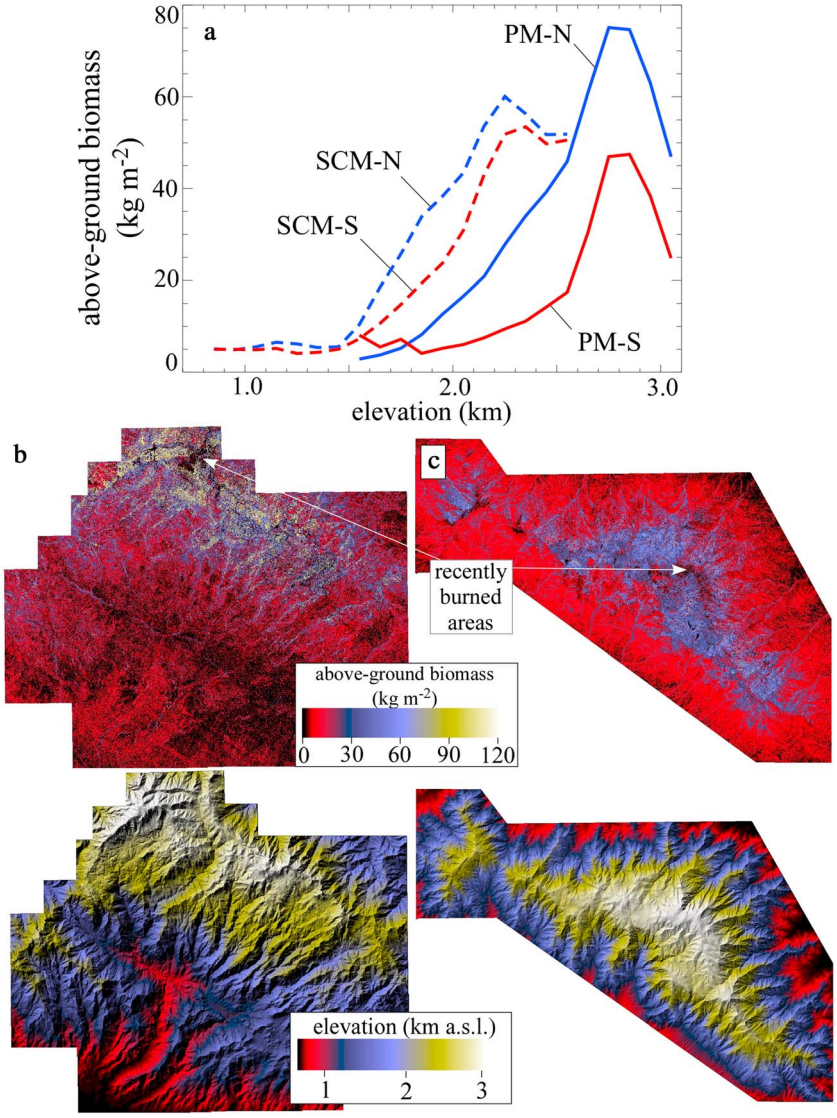

Figure 4. (a) Plots of mean above-ground live dry biomass (AGB) versus elevation for north- and south-facing slopes in SCM and PM. Color maps of above-ground biomass in (b) SCM and (c) PM. Shaded-relief images of the topography within the areas of airborne lidar coverage are also shown.

indicate that AGB in SCM and PM increases in a strongly nonlinear way with both elevation/EEMT and that north-facing slopes have significantly more biomass than south-facing slopes.

3.4. Mean Distance-to-Valley

[18] To compute the distance-to-valley metric, hillslopes and valleys must first be distinguished in high-resolution, bare-earth DEMs. Once each pixel is identified as a hillslope (e.g., a portion of the landscape undissected by localized fluvial pathways) or a valley (a zone of localized, concentrated surface water flow), the distance from every pixel to the nearest valley along the path of steepest descent (identified using the D8 routing algorithm) is computed to provide a map of the distance-to-valley, a variable that is inversely proportional to drainage density [*Tucker et al.*, 2001]. That map can then be averaged in 100 m elevation bins to obtain the mean distance-to-valley as a function of elevation and slope aspect.

[19] Most existing methods for distinguishing hillslopes and valleys in high-resolution lidar DEMs rely to one extent or another on contributing area as a mapping criterion, with areas of larger contributing area classified as valleys (perhaps based on additional criteria besides contributing area) and areas of lower contributing area classified as hillslopes. This is problematic because it guarantees that portions of the landscape with large contributing areas will be classified as valleys regardless of their morphology, i.e., whether or not they are dissected portions of the landscape. To solve this problem, *Pelletier* [2013] developed a technique for drainage network identification that uses only contour curvature (i.e., the curvature of contour lines) to distinguish hillslopes from valleys. In this method, a lidar-derived bare-earth DEM is filtered to remove small-scale noise, contour curvature is computed, and valley heads are identified as the areas closest to the divides where the contour curvature rises above a user-defined threshold value (nominally 0.1 m^{-1}). Once valley heads are identified, a multiple-flow-direction routing technique is used to map the valley downstream from the valley head. *Pelletier* [2013] obtained accurate results using this method for two very different landscapes (one in SCM) using the same user-defined threshold value, thereby demonstrating the robustness of the technique.

[20] Mean distance-to-valley increases nonlinearly with elevation from a low value of approximately 20 m to a maximum of approximately 130 m in SCM (Figure 5). The highest elevations of PM continue the nonlinear trend present in the higher elevations of SCM, with mean

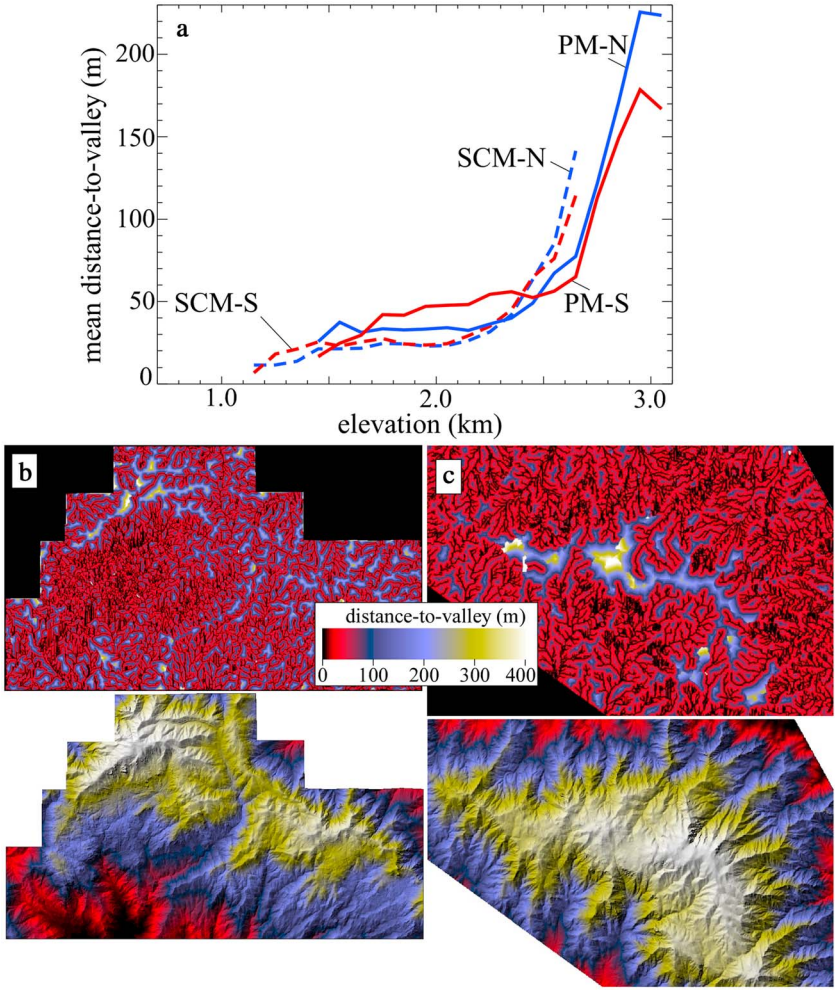

Figure 5. (a) Plots of mean distance-to-valley versus elevation for north- and south-facing slopes in SCM and PM. Color maps of distance-to-valley in the central portions of (b) SCM and (c) PM.

distance-to-valley values reaching 200 m at the highest elevations. The data show relatively little difference between north- and south-facing slopes. This lack of slope-aspect control is perhaps surprising given the strong slope-aspect controls on EEMT and AGB, a point to which we will return to in section 5.

3.5. Relief

[21] Topographic relief, defined as the elevation difference between the highest and lowest pixels within a given radius from each point, is straightforward to map using DEMs. Relief tends to increase with scale, i.e., the distance from each point over which the maximum and minimum are determined; hence, a scale must be chosen for the mapping that is consistent with the scientific questions addressed by the analysis. Here we use a 50 m search radius, equivalent to a 100 m spatial scale, because our goal is to quantify steepness at the hillslope scale. At scales much larger than 100 m, i.e., watershed scales, relief is primarily controlled by the erosivity of fluvial channels since watershed-scale relief is controlled primarily by along-channel slopes within the fluvial network and such slopes are controlled primarily by the resistance of the substrate to fluvial erosion. A 100 m scale is a reasonable choice for an analysis aimed at quantifying hillslope-scale relief given that the mean distance-to-valley (a proxy for hillslope length) is ~100 m everywhere in the study areas (Figure 5a).

[22] Average relief in SCM ranges from just below 20 m/100 m at low and high elevations to approximately 35 m/100 m at intermediate elevations (approximately 1.7 to 2.7 km asl) (Figure 6). PM shows a similar pattern, except the range is steeper and the relief maximum occurs at a higher elevation, i.e., 2.4 km asl in PM instead of 2.0 km asl for SCM. Relief is greater on north-facing slopes compared to south-facing slopes at intermediate elevations of approximately 1.8–2.6 km asl The greater steepness of north-facing slopes compared with south-facing slopes at intermediate elevations could be a result of geomorphic processes, e.g., higher vegetation cover protecting the hillslope from the combined effect of rain splash and slope-wash erosion, thereby requiring steeper slopes to generate similar slope-wash erosion rates on north-facing hillslopes versus south-facing hillslopes [*Yetemen et al*., 2010; *Dunne et al*., 2010]. However, it is difficult to rule out tectonic and structural influences as factors controlling the aspect differences illustrated in Figure 6. During Oligo-Miocene extension, relief in SCM and PM was produced along low-angle detachment faults on the south and north sides of each range, respectively. In SCM, this resulted in south-ward tilting of the range and the development of an extension-parallel structural fabric in the bedrock (especially at lower elevations). Both of these processes likely resulted in initial slopes and/or rates of soil production that depend on slope aspect and could have played a significant role in the development of aspect-controlled differences in relief.

3.6. Soil Thickness

[23] Mean soil thickness, defined here as the depth to the paralithic contact, increases nonlinearly with elevation; i.e., soil thickness increases gradually with elevation from approximately 0.1–0.3 m at 1 km asl to 0.4 m at 2 km asl, then more abruptly from 0.4 m at 2 km asl to 0.8 m at 2.4 km asl Data plotted in Figure 7 were acquired from five north-facing sites across the elevation/climate gradient in SCM. Data from divergent and convergent (i.e., hollow) topographic positions were averaged to obtain a single representative soil thickness for each site [*Lybrand et al*., 2011]. It should be noted that the data plotted in Figure 7 differ slightly from those of *Lybrand et al*. [2011]. The difference is related to the fact that there was some variability across elevation sites in terms of how the depth to paralithic contact was defined in *Lybrand et al*. [2011]. The data plotted in Figure 7 represent the depth to paralithic contact defined consistently as the depth to a consolidated Cr horizon.

[24] The empirical analysis of this section quantified the correlations among EEMT, vegetation cover, soil thickness, and topographic variables across the elevation/climate gradient of SCM and PM. In section 4, we introduce a numerical model aimed at understanding the feedback relationships that give rise to these correlations.

4. Numerical Modeling

4.1. Soil Production From Bedrock

[25] Hillslopes in upland environments evolve predominantly via a combination of bedrock weathering (which produces regolith) and colluvial transport (which erodes it).

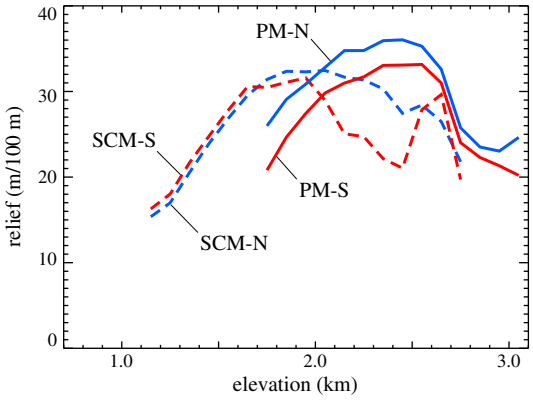

Figure 6. Plots of mean relief (at 100 m scale) versus elevation for north- and south-facing slopes in SCM and PM.

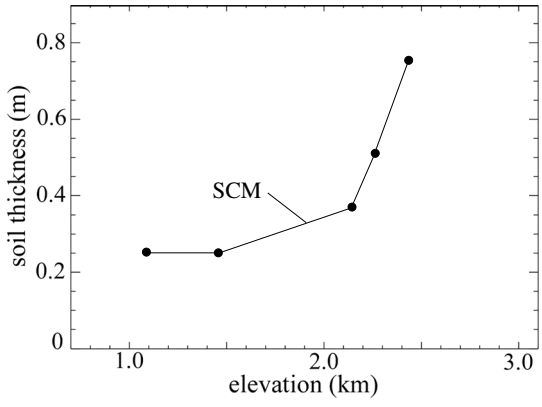

Figure 7. Plot of soil thickness versus elevation on north-facing slopes in SCM.

For hillslopes in arid and semi-arid environments with non-$CaCO_3$-rich bedrock, the physical weathering of bedrock into regolith is typically 80% or more of total weathering [*Riebe et al*., 2004; *Rasmussen*, 2008]. In our model, the thickness of regolith on upland landscapes is controlled by the long-term balance between rates of physical bedrock weathering and erosion. This balance can be quantified as

$$z = b + h \tag{6}$$

$$\frac{\partial b}{\partial t} = U - \frac{P}{\cos\theta} \tag{7}$$

$$\frac{\partial h}{\partial t} = \frac{\rho_b}{\rho_s}\frac{P}{\cos\theta} - E \tag{8}$$

where z is the elevation of topography, b is the elevation of the underlying weathering front or bedrock surface, h is the regolith thickness, ρ_b is the bedrock density, ρ_s is the bulk regolith density, P is the rate of bedrock recession normal to the surface, θ is the slope angle, U is the rock uplift rate, and E is the erosion rate [*Heimsath et al*., 1997; 2001; *Minasny and McBratney*, 1999].

[26] Cosmogenic radionuclide (CRN) studies indicate that the rate of bedrock recession by physical weathering normal to the surface decays exponentially with the thickness of overlying soil measured normal to the surface, $h\cos\theta$, i.e.,

$$P = P_0 e^{-h\cos\theta/h_0} \tag{9}$$

where P_0 is the potential weathering or bare-bedrock recession rate and h_0 is a constant equal to approximately 0.5 m based on data from the studies of *Heimsath et al*. [1997, 2001]. Theoretical studies suggest that a humped relationship of soil/regolith production to thickness may be appropriate in some cases [e.g., *Anderson and Humphrey*, 1989; *Strudley et al*., 2006]. Recent cosmogenic radionuclide data provide support for a humped production model [e.g., *Heimsath et al*., 2009; *Wilkinson and Humphreys*, 2005], but here we use the exponential model because the functional form of the humped model is still not well constrained by available data.

[27] The value of P_0 depends on climate and parent material. *Rasmussen and Tabor* [2007] found that regolith thickness on slowly eroding granitic hillslopes in the Sierra Nevada increases exponentially with EEMT, suggesting that rates of regolith production also increase exponentially with EEMT, i.e.,

$$P_0 = ae^{b\cdot EEMT} \tag{10}$$

where a (units of m kyr^{-1}) and b (units of m^2 yr kJ^{-1}) are empirical coefficients. *Pelletier and Rasmussen* [2009a] constrained the parameters a and b in equation (10) for granitic landscapes using published data from *Riebe et al*. [2004] and obtained best-fit coefficients $a = 0.037$ m kyr^{-1} and $b = 0.03$ m^2 yr MJ^{-1}. The resulting values of P_0 are in the range of 0.04–0.10 m kyr^{-1} for a wide range of arid to sub-humid climates, with larger values generally limited to warm, humid climates. However, it should be emphasized that equation (10) and the particular values of a and b used here are not universal even for a single rock type. Regolith production rates depend on the join/fracture density of the rock; hence, granite with unusually high fracture densities could be characterized by P_0 values higher than 0.10 m kyr^{-1} even in relatively dry climates.

4.2. Colluvial Transport

[28] Erosion on hillslopes and in low-order fluvial valleys occurs by flowing water (e.g., slope wash and channel flow) and colluvial processes (e.g., creep, bioturbation) if soil is present. Erosion/deposition by colluvial processes is related to the divergence of the flux of regolith/soil via mass conservation, i.e.,

$$E_c = \nabla\cdot\mathbf{q} \tag{11}$$

where E_c is the erosion/deposition rate due to colluvial processes (defined as positive if soil is being removed) and $\mathbf{q}$ is a volumetric sediment flux. Early research on modeling colluvial transport [*Culling*, 1960; 1963] assumed that the flux of soil or regolith was proportional to the slope gradient, i.e.,

$$\mathbf{q} = -\kappa\nabla z \tag{12}$$

where κ is a colluvial transport coefficient with units of $length^2$ $time^{-1}$. Combining equations (11) and (12) yields the diffusion equation for soil-mantled hillslopes. As slopes steepen, however, the linear relationship between flux and gradient assumed in equation (12) breaks down. *Roering et al*. [1999, 2004], following upon *Andrews and Bucknam* [1987], proposed a nonlinear slope-dependent transport model given by

$$\mathbf{q} = -\frac{\kappa\nabla z}{1 - (|\nabla z|/S_c)^2} \tag{13}$$

where S_c is the critical slope gradient at which sediment flux goes to infinity. Equations (12) and (13) are limited, however, in that they exhibit an unrealistic discontinuity in flux as the soil thickness goes from zero to some finite value. An alternative approach is to assume that the flux is proportional to the soil thickness measured normal to the tangent of the slope for relatively thin soils (i.e., less than ~1 m):

$$\mathbf{q} = -\frac{\kappa_d h\cos\theta\nabla z}{1 - (|\nabla z|/S_c)^2} \tag{14}$$

where κ_d has units of $length^1$ $time^{-1}$ [*Furbish et al*., 2009; *Roering*, 2008]. In this paper, we adopt equation (14) to model the colluvial sediment flux based on the fact that depth-dependent transport has been shown to lead to more accurate predictions of soil thickness in well-constrained field cases [e.g., *Heimsath et al*., 2005; *Pelletier et al*., 2011]. The coupling between soil thickness and colluvial sediment transport is included via the h dependence on the right side of equation (12). The climatic and vegetative control on colluvial sediment flux will be included in equation (12) by making κ_d a function of EEMT and AGB.

[29] Here we assume that the h in equation (14) is the same as the h in equation (9). This assumption is based on the relative paucity of saprolite in the granitic soils of SCM and PM. An alternative approach developed by *Crouvi et al*. [2013] is to use the field-measured average ratio of soil thickness to regolith thickness to scale the value of h in equation (14) to honor the fact that the average thickness of mobile regolith may be somewhat less than the thickness of all regolith.

[30] The geomorphic literature contains few quantitative constraints on how κ varies with climate. Two lines of evidence, however, suggest that values of κ increase in more humid climates and/or in areas of higher vegetation density. First, *Hanks* [2000] compiled data on values of κ inferred from the degradation of landforms of known age (e.g., pluvial shoreline scarps). The values of κ reported by *Hanks* [2000] increase systematically in more humid climates: i.e., $\kappa = 0.1$–0.7 m^2 kyr^{-1} in the hyperarid and arid portions of Israel, $\kappa = 0.5$–2.0 m^2 kyr^{-1} in the semi-arid portions of the western U.S., and $\kappa \geq 10$ m^2 kyr^{-1} in coastal California and Michigan. One limitation of scarp studies is that they most often constrain the long-term values of κ in cases where an abundance of soil is available for transport. Effective diffusivity values may be lower in upland environments where soil is supply limited. Second, *Hughes et al*. [2009] inferred a near doubling of colluvial transport rates in a landscape of moderate relief in New Zealand between the late Pleistocene and early Holocene, coincident with a shift to a Holocene forest ecosystem (e.g., a higher vegetation density). The results of *Hughes et al*. [2009] are consistent with a series of papers that relate the value of κ directly to vegetation density [*Roering et al*., 2004; *Walther et al*., 2009]. Rates of sediment transport by bioturbation can be expected to increase with increasing vegetation density because more plants are available to drive transport [*Gabet et al*., 2003].

[31] The effects of a wetter climate and/or greater vegetation cover on rates of colluvial sediment transport are included in the model via the equation

$$\kappa_d = cEEMT + dAGB \tag{15}$$

where c and d are empirical coefficients. The conceptual model underlying equation (15) is illustrated in Figure 8a. We assume that colluvial sediment transport is driven by a combination of creep (represented by the first term on the right side of equation (15)) and bioturbation (represented by the second term on the right side). Creep rates can be expected to increase linearly with EEMT in water-limited environments, because EEMT also increases approximately linearly with water availability in such environments and water/soil moisture is a necessary component of the freeze/thaw cycles that drive creep. Rates of bioturbation-driven sediment transport can, to first order, be expected to increase linearly with AGB. The values of the coefficients c and d are chosen so that equation (15) yields values for κ_d consistent with values reported in the literature for a range of different climates. Such calibration can only be done in an approximate way given our relatively imprecise knowledge of how κ_d values depend on climate. Here we assume that the value of κ_d has a low value of approximately 0.3 m kyr^{-1} at the lowest elevations in the sky islands, increasing to approximately 3 m kyr^{-1} at the highest elevations. As noted above, inferred values of κ are in the range 0.1 to 1 m^2 kyr^{-1} in arid climates such as those of the Sonoran Desert. This is equivalent to κ_d values in the range of 0.1 to 1 m kyr^{-1}, assuming a characteristic soil thickness ~1 m. As such, we take 0.3 m kyr^{-1} to be a representative low elevation values for κ_d. Conversely, at high elevation/more-humid climates we assume that κ_d values increase to 3 m kyr^{-1}. This

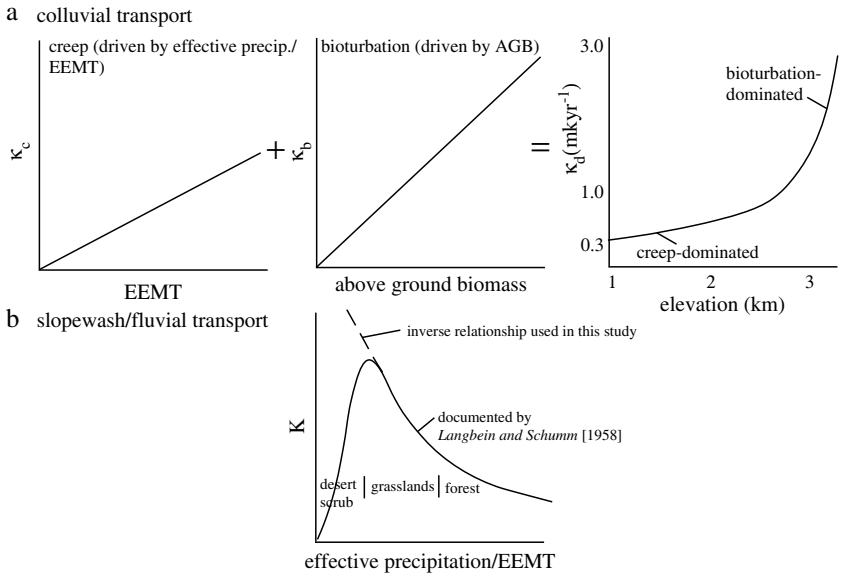

Figure 8. Schematic illustration of climatic and vegetative control of colluvial and fluvial transport rates in the model. (a) The rate of colluvial transport is assumed to be a superposition of a creep-driven component (proportional to EEMT) and a bioturbation-driven component (proportional to above-ground biomass). The coefficient of colluvial transport, κ_d, is calibrated to match coefficients of colluvial transport corresponding to semi-arid locations at low elevation (where colluvial transport is assumed to be creep-dominated) and relatively humid locations at high elevation (where colluvial transport is assumed to be bioturbation-dominated). (b) The rate of slope-wash/fluvial transport is assumed to be an inverse function of EEMT, broadly consistent with the trend documented by *Langbein and Schumm* [1958].

value is intermediate between those of semi-arid climates (i.e., $\kappa = 0.5$–2.0 m^2 kyr^{-1}) and humid climates, e.g., coastal California (i.e., $\kappa = 10$ m^2 kyr^{-1}) [*Hanks*, 2000]. Given these end-member estimates for κ_d at low elevations (where creep-driven colluvial transport dominates because biomass is low) and high elevations (where bioturbation-driven colluvial transport dominates because biomass is high), estimates for c and d can be determined. Values of c and d estimated in this way were determined to be $c = 0.033$ m^4 MJ^{-1} and $d = 0.05$ m^4 MJ^{-1} kyr^{-1}.

4.3. Slope-Wash/Fluvial Transport

[32] Slope-wash/fluvial transport is the transport of sediment that occurs by water flowing over the landscape, either as the unconcentrated sheet flow of water on hillslopes or the concentrated flow of water in valley bottoms. Here we use the stream-power model to quantify this type of erosion, i.e.,

$$E_f = K\frac{A}{w}|\nabla z| \tag{16}$$

where E_f is the erosion rate due to slope-wash/fluvial processes, K is an erodibility coefficient (units of kyr^{-1}), A is contributing area, and w is the effective width of flow (equal to the pixel width, Δx, if flow is by sheet flooding or equal to the valley bottom width if flow is confined to the valley bottom). The linear form of the stream-power erosion model is used here for simplicity. It should be noted that although equation (16) is perhaps best known for its ability to model erosion in bedrock channels by the process of plucking, in this paper it is used to model the detachment-limited erosion of regolith on hillslopes, in hillslope hollows, and in low-order valleys that generally have colluvial deposits present. High-order valleys with well-defined bedrock channels do not occur in the model because valleys have a maximum contributing area of 1 km^2.

[33] In tributary valleys, it is often a good approximation to assume that the valley-bottom width is proportional to a power function of the contributing area (a proxy for discharge), i.e.,

$$w = gA^i \tag{17}$$

where $i \approx 1/2$ and g is a dimensionless coefficient that varies between drainage basins [*Leopold and Maddock*, 1953]. In the model results of this paper, we assume $i = 1/2$ and $g = 0.005$. The value of g was chosen to match field measurements in SCM and PM; i.e., they predict valley-bottom widths consistent with valley widths observed in the field in these ranges (e.g., $w \approx 0.5$ m in drainage basins with contributing areas ~10^4 m^2 and $w \approx 5$ m in drainage basins with contributing areas ~1 km^2). In the model, we apply equation (16) using two different values of K: a relatively large value that represents the resistance of regolith to slope-wash/fluvial erosion (applied if regolith is present) and a relatively small value (applied if regolith is not present) that represents fluvial erosion into bedrock. The ratio of the coefficient of erodibility of regolith to that of bedrock is defined as F. The erosion quantified by equation (16) is added to the erosion/deposition that occurs by colluvial processes (i.e., equation (11)) to obtain the total erosion for each point on the landscape. On hillslopes (where A is low), erosion by colluvial processes dominates (i.e., the erosion from equation (11) is greater than the erosion from equation (16)), while in valleys, the opposite is true [*Tucker and Bras*, 1998; *Perron et al.*, 2008]. In this study, the effects of climate on slope-wash/fluvial erosion are included by varying the two values of K with climate in a way that is consistent with sediment yield-climate relationships published in the literature. It should be noted that a threshold for detachment may be added to equation (16), but *Perron et al.* [2008] found that the presence or absence of a detachment threshold does not substantially affect the valley spacing or drainage density produced by a landscape evolution model that uses equation (16) [e.g., *Perron et al.*, 2008, Figure 13].

[34] *Langbein and Schumm* [1958] compiled data on the average sediment yield from small drainage basins in the western U.S. and analyzed those data in terms of effective precipitation. *Langbein and Schumm* [1958] found that sediment yield increases, on average, with increasing mean annual effective precipitation in the range from 0 to approximately 0.3 m yr^{-1} (i.e., environments with desert scrub vegetation) and then decreases with increasing mean annual effective precipitation for values above 0.3 m yr^{-1} (i.e., environments transitional from desert scrub to grassland, grassland, and forest). In the arid to semi-arid range of 0 to 0.3 m yr^{-1}, vegetation cover is relatively low and increasing precipitation has the effect of liberating more sediment and conveying more of that sediment off the hillslope in overland-flow producing events. As the mean annual effective precipitation increases further, however, the increasing vegetation cover that accompanies a more humid climate has the effect of reducing the sediment yield. For these relatively wet climates, the tendency of vegetation to increase sediment yield via rain splash detachment and runoff from hillslopes, hillslope hollows, and low-order valleys with colluvial deposits is negated by the effect of having more vegetation anchoring the soil. The resistance to erosion provided by plant cover is by far the most important control on K in such environments, unlike in bedrock channels where erosive power (and hence values of K) generally increases with increasing mean annual precipitation. In this study, we quantify the inverse relationship between sediment yield and effective precipitation in an approximate way by assuming an inverse proportionality between the slope-wash/fluvial regolith erodibility coefficient K and *EEMT*, i.e.,

$$K = K_0/EEMT, \tag{18}$$

where K_0 is a constant (units of m^2 MJ^{-1}). It is not necessary to model both sides of the peak in the Langbein-Schumm curve because all of the portions of SCM and PM considered in this study are subject to mean annual effective precipitation in excess of approximately 0.3 m yr^{-1}. Equation (18) is used in the model to quantify the rate of fluvial erosion into bedrock (if all available regolith has been removed), but the value of K_0 is decreased by the factor F to reflect the increased resistance of bedrock to fluvial erosion compared to regolith. The value of K_0 is treated as a free parameter in the model and is varied to produce landscapes with drainage densities in the range of those observed in SCM and PM for a given EEMT value. It should be noted that other studies have questioned the Langbein-Schumm curve in some respects [e.g., *Wilson*, 1973]. However, nearly all studies that have examined the relationship between

sediment yield and climate have concluded that an inverse relationship exists between sediment yield and mean annual effective precipitation for climates with precipitation in excess of approximately 0.3 m yr^{-1}.

4.4. Numerical Model Implementation

[35] The numerical model solves for the topography and soil thickness corresponding to an approximate topographic steady-state condition driven by a prescribed uniform bedrock uplift rate. The sky islands of southern Arizona are no longer subject to active tectonic uplift, but bedrock does still move vertically in response to erosional unloading and the resulting flexural-isostatic response of the lithosphere [e.g., *Pelletier*, 2010a]. Near a topographic steady-state condition, the rate of rock uplift will, by definition, be balanced by the rate of erosion.

[36] *Rasmussen* [2008] estimated erosion rates using ^{10}Be concentrations at the saprolite-bedrock interface from divergent hillslopes in the Rincon Mountains (adjacent to SCM and part of the Catalina-Rincon metamorphic core complex) at a range of elevations. The CRN-constrained physical erosion rates he obtained ranged from 60 to 120 g m^{-2} yr^{-1}, but two of the three samples were approximately 120 g m^{-2} yr^{-1}, equivalent to a bedrock lowering rate of approximately 0.05 m kyr^{-1}, assuming a bedrock specific gravity of 2.6. In our model, we force the landscape with a bedrock uplift rate of $U = 0.05$ m kyr^{-1}, consistent with the upper end of the range of values obtained by *Rasmussen* [2008].

[37] Climate in the model is prescribed via a value of EEMT, assumed to be uniform within the model domain. The calculation of EEMT includes the seasonality of temperature and precipitation, but actual seasons are not resolved in the model. In nature, EEMT varies as a function of elevation and slope aspect (Figure 3). However, for simplicity, we use one value for EEMT throughout the model domain. EEMT varies relatively little over elevation ranges of less than 300 m (the maximum relief obtained in our model experiments); hence, it is a reasonable approximation to assume that EEMT is uniform at the spatial scale (i.e., ~1 km^2) represented by our model. A more complex version of the model could be used that modifies EEMT dynamically with slope and aspect. When applying the results of the model qualitatively to the landscapes of SCM, areas of higher elevation have higher EEMT, and at a given elevation, north-facing slopes have higher EEMT compared to south-facing slopes.

[38] The numerical model domain is a 10 m/pixel 101 × 201 raster grid that begins with an initially low-relief landscape (one that barely drains water to the boundaries without ponding) with no soil cover. The boundary conditions are periodic in the short dimension and fixed at zero along non-uplifting base-level boundaries in the long dimension, thus mimicking two drainage basins separated by a central ridgeline. The model accepts, as input, a prescribed value of EEMT, which is varied in nine different model runs from 5 MJ m^2 yr^{-1} to 45 MJ m^2 yr^{-1} in increments of 5 MJ m^2 yr^{-1}. Within a given model run, EEMT is uniform and the model produces characteristic topographic (i.e., mean relief and distance-to-valley) and soil variables for that model run. Between model runs, EEMT is varied (as a proxy for a change in the mean elevation of the catchment) and this results in variations in characteristic topographic and soil variables between one model run and another. EEMT vary with aspect as well as elevation, but since elevation is by far the stronger of the two controls (e.g., Figure 3), it is reasonable to vary EEMT in the model to represent different mean elevations along the elevation/climate gradient. All other parameter values are held fixed across all model runs (Table 1); hence, all of the differences in model output can be attributed to differences in EEMT. The value of EEMT is used to estimate the value of AGB based

Table 1. Input Parameters of the Numerical Model

Symbol	Definition	Value(s) (Dimensionless If No Units Given)	Basis for Value(s)
a	Empirical coefficient relating P_0 and EEMT in granitic rocks	0.037 m kyr^{-1}	*Pelletier and Rasmussen* [2009a]
b	Empirical coefficient relating P_0 and EEMT in granitic rocks	0.03 m^2 yr MJ^{-1}	*Pelletier and Rasmussen* [2009a]
c	Empirical coefficient relating κ_d and EEMT in sky islands	0.033 m^4 MJ^{-1}	Empirical correlation between EEMT and literature-based estimates of κ_d
d	Empirical coefficient relating κ_d and AGB in sky islands	0.05 m^4 MJ^{-1} kyr^{-1}.	Empirical correlation between AGB and literature-based estimates of κ_d
ε	empirical coefficient relating AGB and EEMT in sky islands	1 kg m^{-2}	Empirical correlation using lidar and EEMT model
EEMT	Effective energy and mass transfer	varied from 5–45 MJ m^{-2} yr^{-1} in increments of 5 MJ m^{-2} yr^{-1}	Equation (1)
f	Empirical coefficient relating AGB and EEMT in sky islands	0.1 yr m^2 MJ^{-1}	Empirical correlation using airborne lidar data and EEMT model
F	Ratio of the slope-wash/fluvial erodibility coefficient of regolith to that of bedrock	10	No firm basis, but model results insensitive to this parameter
g	Empirical coefficient relating width of flow in valley bottom to contributing area	0.005	Empirical correlation to field-measured valley-bottom widths
h_0	Length scale in soil production function	0.5 m	*Heimsath et al.* [1997; 2001]
i	Empirical coefficient relating width of flow in valley bottom to contributing area	0.5	*Leopold and Maddock* [1953]
K_0	Empirical coefficient relating coefficient of slope-wash/fluvial erodibility of regolith to EEMT	0.02 m^2 MJ^{-1}	Calibrated to match observed mean distance to valley at EEMT = 10 MJ m^{-2} yr^{-1}
ρ_b/ρ_s	Density ratio of bedrock to regolith	1.8	Standard value for granitic bedrock/regolith
S_c	Gradient of hillslope stability	0.7	Typical value for angle of repose
U_0	Rock uplift rate	0.05 m kyr^{-1}	*Rasmussen* [2008]

on the empirical correlation in equation (5). The values of EEMT and AGB control rates of soil production, colluvial transport, and slope-wash/fluvial transport in the model according to equations (10) and (15)–(18). The value of K_0 was chosen to be 0.02 m^2 MJ^{-1} (using a trial-and-error procedure) based on the fact that this value yields a mean distance-to-valley value that matches the measured mean distance-to-valley at the low elevations of SCM and PM (i.e., at elevations corresponding to EEMT = 10 MJ m^{-2} yr^{-1}). Drainage density is controlled primarily by the ratio of the colluvial transport coefficient to the fluvial transport coefficient [*Tucker and Bras*, 1998; *Perron et al*., 2008]. Therefore, given a value for the colluvial transport coefficient, an appropriate value for the fluvial transport coefficient K_0 can be obtained by varying the value of K_0 until a realistic drainage density is achieved for some reference value of EEMT as we have done. The fact that the model reproduces realistic drainage densities/mean distances-to-valley at EEMT = 10 MJ m^{-2} yr^{-1} cannot be considered to be a success of the model because the model is tuned to match observed data for this value of EEMT. However, the fact that the model reproduces the observed nonlinear increase in mean distance-to-valley across the EEMT gradient can be considered to be a successful match of the model to data. The value of F (the relative erodibility of regolith to bedrock by slope-wash/fluvial processes) was chosen to be 10 for the results presented in this paper, but quantitatively similar results were obtained for a range of values of F from 10 to 100. The value for S_c was chosen to be 0.7 (35°) based on the typical angle of repose for unconsolidated material. Values of S_c reported in the literature are often higher than 0.7; hence, we reran the model with an S_c value of 0.9 to test the robustness of the results to uncertainty in this value. The model predictions for relief, soil thickness, and mean distance-to-valley differed by less than 10% compared to the values obtained with $S_c = 0.7$.

[39] Soil production during each time step and within each pixel is computed using Euler's method; i.e., during each time step, the soil thickness at the beginning of the time step is used to compute the increase in soil thickness during that time step due to soil production as

$$h_{i,j}(t+\Delta t) = h_{i,j}(t) + \Delta t \frac{\rho_b}{\rho_s}\frac{P_0}{\cos\theta} e^{-h(t)\cos\theta/h_0} \tag{19}$$

[40] Erosion and deposition in the model is computed using the Forward-Time-Centered-Space (FTCS) method. The x and y components of the colluvial sediment flux in the FTCS method are computed using the elevation and soil thickness values at time step t via the equations

$$q_{x_{i+1/2,j}} = -\kappa_d \frac{1}{2}\left(h_{i+1,j} + h_{i,j}\right)\frac{z_{i+1,j} - z_{i,j}}{\Delta x\left(1 - \left(\left(z_{i+1,j} - z_{i,j}\right)/\left(\Delta x \cdot S_c\right)\right)^2\right)} \tag{20}$$

and

$$q_{y_{i,j+1/2}} = -\kappa_d \frac{1}{2}\left(h_{i,j+1} + h_{i,j}\right)\frac{z_{i,j+1} - z_{i,j}}{\Delta x\left(1 - \left(\left(z_{i,j+1} - z_{i,j}\right)/\left(\Delta x \cdot S_c\right)\right)^2\right)} \tag{21}$$

[41] Fluxes computed by equations (20) and (21) are indexed at half grid points because fluxes are not defined at any grid point but rather as the sediment flowing between two grid points. Conservation of mass is given by

$$h_{i,j}(t+\Delta t) = h_{i,j}(t) - \frac{\Delta t}{\Delta x}\left(q_{x_{i+1/2,j}} - q_{x_{i-1/2,j}}\right) - \frac{\Delta t}{\Delta x}\left(q_{y_{i,j+1/2}} - q_{y_{i,j-1/2}}\right) \tag{22}$$

[42] To maintain stability, the model time step must be less than $(\Delta x)^2/2\kappa$ (i.e., the Courant stability criterion) for a slope-dependent transport model (i.e., topographic diffusion) and much less than that for the depth- and nonlinear-slope-dependent model. In our model, we employed a default time step that was one hundred times lower than this upper limit, i.e., 0.01 $(\Delta x)^2/2\kappa_d$, but we also allowed the time step to vary dynamically such that the maximum amount of erosion or deposition was not allowed to be greater than a small threshold value during any time step. More sophisticated implicit techniques are available for solving the depth- and nonlinear-slope-dependent transport equation that allow for longer time steps [e.g., *Perron*, 2011], but we found explicit time stepping to be adequate for this project given the modest grid sizes. We verified convergence in all cases by rerunning the model with the threshold value set to half the value of the previous run and verified that the difference in soil thickness and topography near steady state between the two models with was at most a few centimeters. Also, we varied the pixel size by a factor of 5 and verified that the model results did not change significantly over that range of spatial resolutions.

[43] The fluvial erosion component of the model requires that an effective width of flow be specified for every pixel (i.e., w in equation (16)). In tributary valleys, w is a function of contributing area, and A can be calculated using standard flow-routing algorithms in a manner that does not depend sensitively on grid resolution. On hillslopes where sheet flooding occurs, however, contributing areas depends directly on DEM resolution. Here we use the approach of *Pelletier* [2010b], who used differences in the grid-resolution dependence of multiple-direction flow routing on hillslopes and in valleys bottoms to differentiate (using a threshold value of the grid-resolution dependence) between hillslopes (where sheet flow is assumed to be distributed throughout each pixel and hence the effective width of flow is equal to the pixel width) and valley bottoms (where flow is confined and equation (17) is used to determine the width of flow). Adopting this or a similar approach is crucial if the goal is to precisely model the transition from hillslopes to valleys (in order to quantify controls on mean distance-to-valley, for example) in a manner that is independent of grid resolution, as discussed by *Pelletier* [2010b].

4.5. Model Results

[44] The model produces landscapes with relatively thin soils and low mean distance-to-valley for low EEMT/elevation cases (Figure 9a for EEMT = 10 MJ m^{-2} yr^{-1}) and relatively thick soils and high mean distance-to-valley for high-EEMT/elevation cases (Figure 9b for EEMT = 40 MJ m^{-2} yr^{-1}). At a given elevation, north-facing slopes have higher EEMT compared with south-facing slopes, so model results with higher EEMT can be used qualitatively to think about how

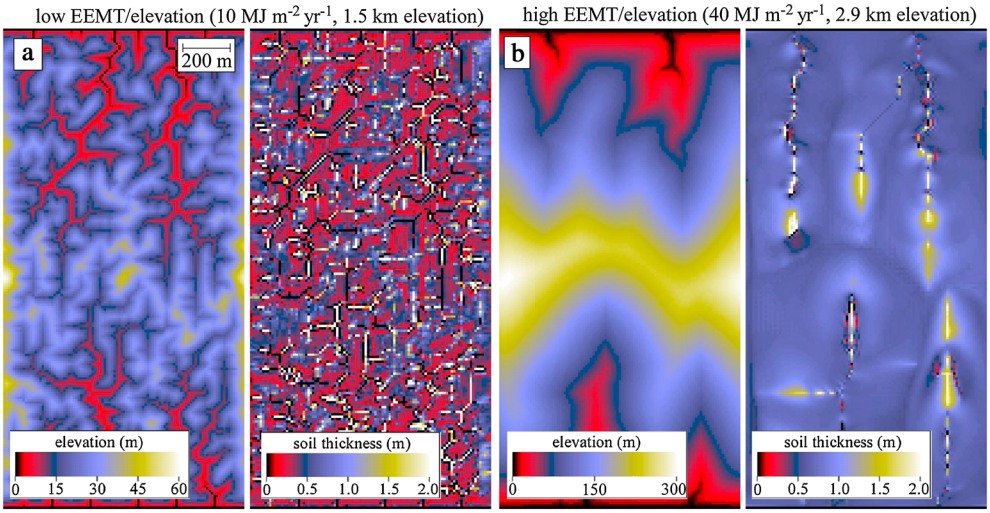

Figure 9. Example output of numerical model, illustrating the sensitivity of soil thickness and mean distance-to-valley to elevation/EEMT. Color maps of topography and soil thickness for a model example with (a) low EEMT (10 MJ m^{-2} yr^{-1}) and (b) high EEMT (40 MJ m^{-2} yr^{-1}). Scale bar shown in Figure 9a also applies to Figure 9b.

landscape properties vary with slope aspect at a given elevation. The model results illustrated in Figure 9 are snapshots of the topography and soil thickness following 10 Myr of uplift, i.e., sufficient time for an approximate dynamic topographic steady state to be achieved for all cases. The model exhibits a *dynamic* topographic steady state because the model exhibits autogenic cut-and-fill cycles along valley bottoms. In the low EEMT case, slopes predicted by the model are steep, mean distance-to-valley is low, and soils on hillslopes are highly variable in thickness but thin on average. As EEMT increases, slopes become progressively less steep, mean distance-to-valley increases, and soils become thicker.

[45] Given the uncertainties inherent in the parameter values used in the model (e.g., the relationship between κ_d and climate) as well as limitations in the empirical data (e.g., soil thickness data from only five sites across the elevation gradient), it is difficult to determine the precise cause and/or significance of relatively small discrepancies between the model and the observed data. As such, we judged the model to be a good fit based simply on the fact that it reproduces the same range of values as the empirical data and the same qualitative trends (i.e., linear versus nonlinear) with elevation as the empirical data (Figure 10). The circles in Figure 10a represent the results of nine individual model runs with EEMT varying from 5 MJ m^2 yr^{-1} to 45 MJ m^2 yr^{-1} in increments of 5 MJ m^2 yr^{-1}. The trends plotted in Figure 10b are average trends for SCM and PM (except for soil thickness, where only data from SCM are available). As such, they do not represent the data for either range precisely but instead represent the average trend of the two ranges.

[46] The model predicts the correct range of soil thicknesses across the elevation gradient, i.e., from approximately 0.25 m to 0.8 m, but the model predicts a more linear increase than is observed in SCM based on the limited data available. Since erosion rates are assumed to be uniform across the range and in balance with rock uplift, the

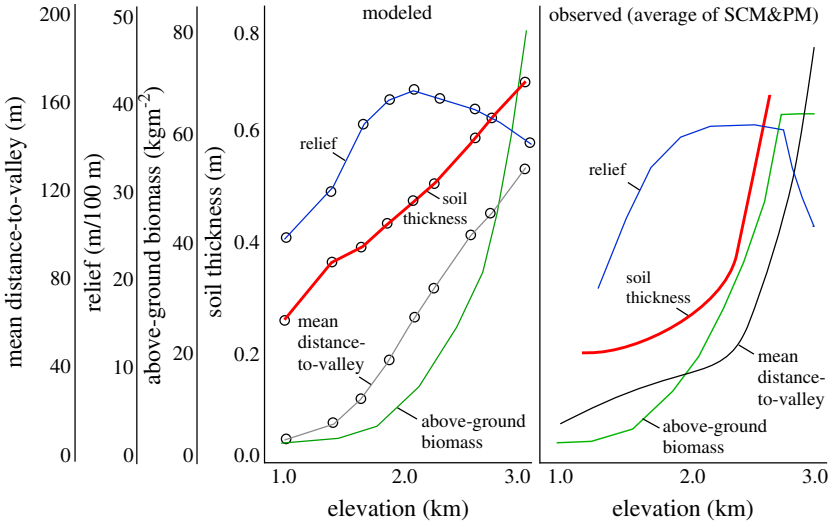

Figure 10. Comparison of (left) model-predicted and (right) measured trends in mean distance-to-valley, relief, above-ground biomass, and soil thickness versus elevation in SCM and PM.

relationship between soil thickness and EEMT principally reflects the increase in soil production rates with increasing EEMT. Soil production increases nonlinearly with EEMT, but soil transport also increases with EEMT, so it is not surprising that soil thickness (which is the difference between production and erosion over geologic timescales) scales more linearly with soil thickness than soil production does.

[47] The model also predicts the correct range and nonlinearity of mean distance-to-valley, i.e., from approximately 10 m at low elevations to >150 m at high elevations of PM. The nonlinear trend in mean distance-to-valley is a consequence of the superposition of two EEMT-related trends that work in concert to lower drainage density: increasing colluvial sediment flux with increasing EEMT and AGB and decreasing fluvial sediment flux with increasing EEMT. Mean distance-to-valley is controlled by the balance between colluvial and fluvial sediment fluxes; hence, any change that simultaneously increases colluvial sediment flux and decreases fluvial sediment flux will drive a nonlinear increase in mean distance to valley.

[48] Hillslope-scale relief in both the model and data increase from a low of approximately 20 m/100 m at low elevations to a high of approximately 40 m/100 m at intermediate elevations. The trend of increasing relief with increasing elevation/EEMT at low elevations is principally related to the increase in mean distance-to-valley that occurs with increasing elevation/EEMT for low elevations. For low-elevation landscapes, the mean distance-to-valley is significantly less than 100 m, thus increasing the mean distance-to-valley increases relief because topographic gradients remain similar but the distance from the divides (local maxima) to the valleys (local minima) increases from a value less than 100 m to a higher value, thereby increasing the relief at the 100 m scale. Relief eventually decreases slightly with increasing elevation/EEMT, however, because average hillslope lengths become comparable to 100 m—hence, any further increase in hillslope length with increasing elevation/EEMT no longer increases the distance between first-order valleys and hence the relief of each hillslope—and because average slopes become slightly lower at higher elevation/EEMT. Slope gradients are slightly lower at high elevation/EEMT because sediment flux is a function of the product of soil thickness and slope, and greater soil thickness means that less slope is required in order for erosion by colluvial transport processes to balance rock uplift.

5. Discussion

[49] Before we discuss the broader implications of our work for understanding critical zone evolution, we first discuss some specific points related to the assumptions and implementation of the numerical model. In the model, regolith thickness along valley bottoms alternates between thick and thin values (Figure 9). These oscillations are likely associated with feedbacks between erosion rate and the effective width of flowing water (i.e., w in equation (16)) in which widening of the valley bottom decreases stream power (and hence erosion rate) in a positive feedback, leading to the development of relatively wide, low-gradient valley-bottom reaches with thick colluvium, alternating with zones of narrower and steeper valley bottoms with thin colluvium. Such oscillations are observed in nature [*Tucker et al*., 2006]. Whether or not a model exhibits such oscillations may depend on the numerical implementation, including the details of how the width of flow on hillslopes and in valley bottoms is computed and how the effective width of flow in valley bottoms is represented. In the model of this paper, the model results are made to be independent of grid resolution using the method of *Pelletier* [2010b], which distinguishes the width of flow on hillslopes (where the effective width of flow depends on DEM resolution) and in valleys bottoms (where it does not). The result is a model in which valley-bottom oscillations are observed. More research is needed to determine the best way to represent the effective width of flow on hillslopes and in valley bottoms and the conditions (both in nature and in models) under which autogenic oscillations occur along valley bottoms. The presence or absence of autogenic oscillations is not crucial for the science questions addressed in this paper; hence, we leave a more detailed study of these oscillations (and how they may or may not arise from the numerical model implementation) to a future paper.

[50] *Heimsath et al*. [1997] developed their soil production function (i.e., equation (9)) to quantify the development of mobile soil only, not saprolite. Regolith is comprised of both mobile soil and relatively immobile saprolite, yet the soil production function has been used in the literature to quantify rates of both soil and regolith development, depending on the objectives of the study. The basis for using the soil production function to quantify regolith development was discussed by *Yoo and Mudd* [2008], who suggested a two-layer model in which equation (9) was applied to the thickening of both soil and regolith (with potentially different values of P_0 and/or h_0). Also, *Lebedeva et al*. [2010] proposed a process-based regolith production model that applies to both mobile soil and relatively immobile saprolite and is consistent with the exponential form in equation (9). The distinction between soil and regolith in the context of equation (9) is significant only in locations where highly weathered saprolite is a substantial component of the regolith profile. Highly weathered saprolite is not a substantial portion of the regolith in SCM and PM; i.e., regolith in the lower elevations of SCM and PM is typically 0.5 m in thickness, i.e., sufficiently thin to be subject to creep-driven transport all the way to bedrock. On gently sloping segments at higher elevations, a 0.3–0.5 m thick creep-driven layer can be distinguished from a less-transportable regolith layer below based on field observations, but at all elevations, the average regolith thickness is < 1 m and hence transportable by landsliding or tree throw (i.e., tree roots commonly extend to > 1 m depths).

[51] *Heimsath et al*. [2012] recently argued that P_0 is a function of erosion rate in addition to climate and rock properties using data from the San Gabriel Mountains. While their results are very intriguing, it is important to note that areas of higher erosion rate in the San Gabriel Mountains tend to be areas of higher elevation where mean annual precipitation (and hence EEMT) is also greater. To our knowledge, *Heimsath et al*. [2012] did not isolate the effects of climate and erosion rate on P_0; hence, there is a possibility that their findings are consistent with a simple dependence of P_0 on climate, i.e., equation (10). It is also important to note that areas of higher erosion rate could have systematically different rock properties (e.g., a higher joint/

fracture density). As such, it may not be erosion rate *per se* that controls P_0 but rather other variables, including fracture density, that have long been known to control P_0 but are nonetheless difficult to quantify at present.

[52] The climate of southern Arizona has fluctuated significantly relative to the modern, especially compared with the Last Glacial Maximum (LGM). The empirical correlations of this paper relate process rates to present-day climates. Given that the LGM climate was significantly cooler and wetter, i.e., capable of supporting a pinyon-juniper woodland at the lowest elevations of SCM and PM [*Van Devender*, 1990], is such a calibration valid? We believe it is valid, to first order, given that (1) the empirical correlations used to calibrate the model also relate process rates over geologic timescales (e.g., κ values) to modern climates and vegetation conditions (e.g., EEMT and AGB), and (2) the *relative* change in climate through time across the elevation gradient has been much smaller than the absolute change; i.e., higher elevations have been cooler and wetter than lower elevations throughout the Quaternary. The potential problem of relic soils is also mitigated in SCM and PM by the fact that erosion rates are sufficiently high that soils are likely to be Holocene in age. Bedrock lowering rates of approximately 5 cm kyr^{-1} [*Rasmussen*, 2008] (equivalent to approximately 9 cm kyr^{-1} of soil erosion given a typical soil/bedrock density contrast of 1.8) imply soil residence times of approximately 4–8 kyr given soil thicknesses of approximately 0.4–0.8 m.

[53] Given the strong influence of aspect on EEMT and AGB, it is perhaps surprising that mean distance-to-valley shows almost no dependence on aspect. One reason for this could be mutually offsetting effects of relief and soil thickness on mean distance-to-valley. North-facing slopes have higher relief than south-facing slopes at intermediate elevations in SCM and PM. All else being equal, higher-relief landscapes tend to have a smaller mean distance-to-valley [*Montgomery and Dietrich*, 1988], although mean distance-to-valley may increase with increasing relief as landsliding become a dominant process [*Oguchi*, 1997]. At the same time, higher EEMT values on north-facing slopes likely increase soil production rates, thereby increasing colluvial transport, which would tend to increase mean distance-to-valley. These two effects might work in opposing ways, resulting in minimal differences in mean distance-to-valley with slope aspect.

[54] Our results highlight the central role played by soil thickness in mediating the feedbacks among vegetation, soils, and topography (Figure 11). Temperature and precipitation (and their joint control on EEMT), in combination with parent material/rock properties, control rates of soil production. The rate of soil production, together with the rate of erosion (which, in gradually declining mountain ranges such as SCM and PM, is balanced by rock uplift), controls soil thickness. Rates of rock uplift also lead to greater relief for otherwise similar conditions, and greater relief leads to thinner soils. Soil thickness, in turn, controls itself via the soil-thickness dependence of the soil production function and the positive relationship between soil thickness and colluvial sediment flux. Greater colluvial sediment flux, all else being equal, leads to thinner soils. The response of soil thickness to perturbations is self-limiting assuming an exponential production function:

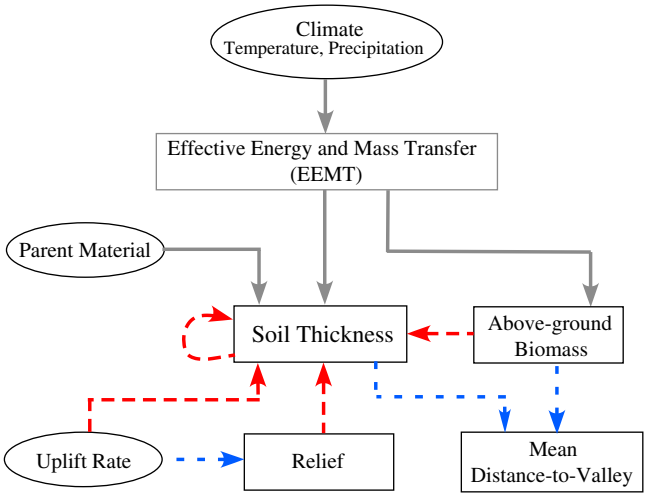

Figure 11. Schematic diagram illustrating feedbacks among vegetation dynamics, pedogenesis, and topographic development assumed in the model, and how those feedbacks are initiated by the inputs of climate (temperature and precipitation), parent material, and uplift rate. Inputs are shown in ovals, while model variables are in rectangles. Positive relationships are shown with blue arrows (an increase in quantity A results in an increase in quantity B, all else being equal) and negative relationships (and increase in A drives a decrease in B) with red arrows.

thicker soils decrease soil production, thereby reducing the local soil thickness for otherwise similar conditions. Increasing soil thickness or active transport depth leads to greater the rate of colluvial sediment transport and hence tends to increase the distance-to-valley as more colluvial sediment fills in low-order fluvial valleys. Increasing AGB also tends to increase distance to valley for the same reason, but the effect of AGB on distance to valley is also enhanced by the fact that more AGB also reduces fluvial erosion, causing the mean distance-to-valley to increase even more than it would otherwise. Increasing AGB tends to reduce soil thickness, since it increases colluvial sediment transport and hence the removal of soil from the hillslope.

[55] Given the strong influence of aspect on EEMT and AGB, it is perhaps surprising that mean distance-to-valley shows almost no dependence on aspect. One reason for this could be the mutually offsetting effects of relief and soil thickness on mean distance-to-valley. North-facing slopes have higher relief than south-facing slopes at intermediate elevations in SCM and PM. All else being equal, higher-relief landscapes tend to have a smaller mean distance-to-valley [*Montgomery and Dietrich*, 1988], although mean distance-to-valley may increase with increasing relief as landsliding become a dominant process [*Oguchi*, 1997]. At the same time, higher EEMT values on north-facing slopes likely increase soil production rates, thereby increasing colluvial transport, which would tend to increase mean distance-to-valley. These two effects might work in opposing ways, resulting in minimal differences in mean distance-to-valley with slope aspect.

[56] It may seem obvious to emphasize the central role of soil thickness in eco-pedo-geomorphic evolution, but many landscape evolution models currently in use do not track

soil thickness explicitly nor do they attempt to quantify the climatic controls on soil production and erosion. For some science questions, it may be adequate to neglect variations in soil thickness across landscapes, but the results of this paper suggest that for many basic questions in climatic geomorphology (e.g., how does drainage density depend on climate?), it is necessary to explicitly track soil thickness and quantify how soil production and erosion depend on readily available climatic variables such as mean annual temperature, precipitation, etc. It should also be noted that soil thickness is just one aspect of the soil that mediates eco-pedo-geomorphic interactions. Another important goal of future research should be to extend this and similar models to predict the evolution of the particle size distribution and hydrologic properties of soils in addition to their thickness. Such models are beginning to be developed [*Crouvi et al*., 2013], but more work is needed.

[57] While the model of this paper is run for the idealized case of uniform block uplift of an initially low-relief landscape, the model could be modified to improve predictions of the variations in soil thickness across real landscapes. *Pelletier and Rasmussen* [2009b], for example, used a simple model of soil production coupled with erosion by depth-dependent colluvial transport (both modeled using uniform parameters) to predict soil thickness across upland hillslopes. The model of this paper includes additional feedbacks that should improve the accuracy of such predictions.

[58] The model of this paper provides only a preliminary quantification of the feedbacks in the critical zone; much more work is needed. As noted in section 4, how vegetation controls soil development and sediment transport processes is still poorly known. At present, we can constrain the relationship between AGB and colluvial sediment transport, for example, only in a semi-quantitative way, i.e., using a model that increases colluvial sediment transport coefficients with increasing EEMT and AGB over a reasonable range (as determined by calibrations of κ or κ_d in different climates) and is consistent with the fact that rates of bioturbation increase in proportion to available water (in water-limited landscapes) and vegetation density. However, whether AGB is the best variable for quantifying vegetation density for the purpose of predicting colluvial sediment transport rates is unknown and more studies aimed at quantifying the relationship between vegetation cover and geomorphic transport rates are needed. The role of water is not explicitly modeled in this paper, in part because water storage varies on the timescales of individual events, i.e., timescales much smaller than the variation in vegetation, soil, or topographic development. Models are needed that quantify the coevolution of CZ processes over geologic time scales yet are still able to resolve individual events. The model of this paper does not consider chemical weathering and its impacts on the hydrologic properties of regolith that derive from its porous media structure. Insofar as the pore structure of the regolith impacts hydrologic partitioning to infiltration and runoff, it might also be expected to impact the relative importance of colluvial versus fluvial erosion.

6. Conclusions

[59] In this paper, we took advantage of the unusually well-defined natural experiment in the coevolution of vegetation, soils, and topography posed by the late Cenozoic evolution of the sky islands of southern Arizona. We compiled high-resolution, spatially distributed data for Effective Energy and Mass Transfer (EEMT) (i.e., the energy available to drive rock weathering), above-ground biomass, soil thickness, hillslope-scale topographic relief, and mean distance-to-valley in the SCM and PM, two predominantly granitic ranges in the sky islands. We showed that strong correlations exist among these variables such that warm, dry, low-elevation portions of these ranges are characterized by low biomass, thin soils, steep slopes, and low mean distance-to-valley. Cooler, wetter, high-elevation portions of these ranges have systematically higher biomass, thicker soils, gentler slopes, and higher mean distance-to-valley. Moreover, all of these variables have a nonlinear dependence on elevation/climate. We developed a landscape evolution model that couples vegetation growth, soil development from bedrock, and topographic evolution by colluvial and fluvial transport over geologic time scales. The model self-organizes into states similar to those observed in SCM and PM for appropriate forcing conditions, i.e., lower biomass and mean distance-to-valley, thinner soils, and higher relief at lower elevations compared to higher elevations. The model provides a preliminary quantification of the feedbacks among vegetation, soil development, and topographic evolution in water-limited environments.

[60] **Acknowledgments.** This study was funded by NSF Award #0724958. We wish to thank Editor Alex Densmore, Associate Editor Simon Mudd, Jill Marshall, Martin Hurst, and one anonymous reviewer for their detailed and constructive reviews.

References

Anderson, R. S., and N. F. Humphrey (1989), Interaction of weathering and transport processes in the evolution of arid landscapes, in *Quantitative Dynamic Stratigraphy*, edited by T. A. Cross, pp. 349–361, Prentice Hall, Englewood Cliffs, New Jersey.

Andrews, D. J., and R. C. Bucknam (1987), Fitting degradation of shoreline scarps by a nonlinear diffusion model, *J. Geophys. Res.*, *92*, 12,857–12,867.

Asner, G. P., J. Mascaro, H. C. Muller-Landau, G. Vieilledent, R. Vaudry, M. Rasamoelina, J. S. Hall, and M. van Breugel (2012), A universal airborne LiDAR approach for tropical forest carbon mapping, *Oecologia*, *168*, 1147–1160.

Briggs, J. C., and C. J. Humphries (2004), Early classics, in *Foundations of Biogeography: Classic Papers with Commentaries*, edited by Lomolino, M. V., and J. H. Brown, pp. 5–13, University of Chicago Press, Chicago.

Brown, J. H., and D. F. Sax (2004), Gradients in species diversity: Why are there so many species in the Tropics? in *Foundations of Biogeography: Classic Papers with Commentaries*, edited by Lomolino, M. V., and J. H. Brown, pp. 1145–1154, University of Chicago Press, Chicago.

Chorover J. et al. (2011), How Water, Carbon, and Energy Drive Critical Zone Evolution: The Jemez-Santa Catalina Critical Zone Observatory, *Vadose Zone J.*, *10*(3), 884–899.

Crouvi, O., J. D. Pelletier, and C. Rasmussen (2013), Predicting soil thickness and the fraction of soil derived from aeolian sediments in upland watersheds of the Mojave Desert, *Geoderma*, *195-196C*, 94–110.

Culling, W. E. H. (1960), Analytical theory of erosion, *J. Geol.*, *68*, 336–344.

Culling, W. E. H. (1963), Soil creep and the development of hillside slopes, *J. Geol.*, *71*, 127–161.

Daly, C., W. P. Gibson, G. H. Taylor, G. L. Johnson and P. Pasteris (2002), A knowledge-based approach to the statistical mapping of climate, *Clim. Res.*, *22*, 99–113.

Davis, G. H., K. N. Constenius, W. R. Dickinson, E. P. Rodriguez, and L. J. Cox (2004), Fault and fault-rock characteristics associated with Cenozoic extension and core-complex evolution in the Catalina-Rincon region, southeastern Arizona, *Geol. Soc. Am. Bull.*, *116*, 128–141.

Dickinson, W. R. (1991), Tectonic setting of faulted Tertiary strata associated with the Catalina core complex in southern Arizona, *Geol. Soc. Am. Spec. Pap. 264*, Boulder, Colorado, 106 p.

Dunne, T., D. V. Malmon, and S. M. Mudd (2010), A rain splash transport equation assimilating field and laboratory measurements, *J. Geophys. Res.*, *115*, F01001, doi:10.1029/2009JF001302.

Etheredge, D., D. S. Gutzler, and F. J. Pazzaglia (2004), Geomorphic response to seasonal variations in rainfall in the Southwest United States, *Geol. Soc. Am. Bull.*, *116*, 606–618.

Furbish, D. J., P. K. Haff, W. E. Dietrich, and A. M. Heimsath (2009), Statistical description of slope-dependent soil transport and the diffusion-like coefficient, *J. Geophys. Res.*, *114*, F00A05, doi:10.1029/2009JF001267.

Gabet, E. J., O. J. Reichman, and E. W. Seabloom (2003), The effects of bioturbation on soil processes and sediment transport, *Ann. Rev. Earth Planet. Sci.*, *31*, 24–273.

Hanks, T. C. (2000), The age of scarplike landforms from diffusion-equation analysis, in *Quaternary Geochronology: Methods and Applications*, edited by J. S. Noller, J. M. Sowers and W. R. Lettis, pp. 313–338, American Geophysical Union, Washington D.C.

Heimsath, A. M., W. E. Dietrich, K. Nishiizumi, and R. C. Finkel (1997), The soil production function and landscape equilibrium, *Nature*, *388*, 358–361.

Heimsath, A. M., W. E. Dietrich, K. Nishiizumi, and R. C. Finkel (2001), Stochastic processes of soil production and transport: Erosion rates, topographic variation and cosmogenic nuclides in the Oregon Coast Range, *Earth Surf. Proc. Landf.*, *26*, 531–552.

Heimsath, A. M., D. J. Furbish, and W. E. Dietrich (2005), The illusion of diffusion: Field evidence for depth-dependent sediment transport, *Geology*, *33*, 949–952, doi: 10.1130/G21868.1.

Heimsath, A. M., G. R. Hancock, and D. Fink (2009), The "humped" soil production function: Eroding Arnhem Land, Australia, *Earth Surf. Processes and Landforms*, *34*, 1674–1684.

Heimsath, A. M., R. A. Dibiase, and K. X. Whipple (2012), Soil production limits and the transition to bedrock-dominated landscapes, *Nature Geosci.*, *5*, 210–214.

Hughes, M., P. Almond, and J. Roering (2009), Increased sediment transport via bioturbation at the last glacial-interglacial transition, *Geology*, *37*, 919–922.

IAEA (2004), Isotope Hydrology Information System, The ISOHIS database Available online at http://isohis.iaea.org.

Istanbulluoglu, E., and R. L. Bras (2005), Vegetation-modulated landscape evolution: Effects of vegetation on landscape processes, drainage density, and topography, *J. Geophys. Res.*, *110*, F02012, doi:10.1029/2004JF000249.

Langbein, W. B., and Schumm, S. A. (1958) Yield of sediment in relation to mean annual precipitation. *Trans. Amer. Geophys. Un. 39*, 1076–1084.

Lebedeva, M. I., R. C. Fletcher, and S. L. Brantley (2010), A mathematical model for steady-state regolith production at constant erosion rate, *Earth Surf. Proc. Landf.*, *35*(5), 508–524.

Leopold, L. B. and T. Maddock Jr. (1953), The hydraulic geometry of stream channels and some physiographic implications, *U.S. Geological Survey Professional Paper 252*, Reston, Virginia, 57 pp.

Lybrand R., C. Rasmussen, A. Jardine, P. A. Troch, and J. Chorover (2011), The effects of climate and landscape position on chemical denudation and mineral transformation in the Santa Catalina mountain critical zone observatory, *Appl. Geochem.*, *26*(S), S80–S84.

McIntosh, R. P. (1986), *The Background of Ecology: Concepts and Theory*, Cambridge University Press, New York, New York.

Merriam, C. H. (1890), Results of a biological survey of the San Francisco Mountains region and desert of the Little Colorado in Arizona, Department of Agriculture, Div. Ornithology and Mammalogy, *N. Am. Fauna*, *3*, 1–136.

Minasny, B., and A. B. McBratney (1999), A rudimentary mechanistic model for soil production and landscape development, *Geoderma*, *90* (1–2), 3–21.

Montgomery, D. R., and W. E. Dietrich (1988), Where do channels begin? *Nature*, *336*, 232–234.

Oguchi, T. (1997), Drainage density and relative relief in humid steep mountains with frequent slope failure, *Earth Surf. Processes and Landforms*, *22*, 107–120.

Pelletier, J. D. (2010a), How do pediments form? A numerical modeling investigation with comparison to pediments in southern Arizona, USA, *Geol. Soc. Am. Bull.*, *122*, 1815–1829.

Pelletier, J. D. (2010b), Minimizing the grid-resolution dependence of flow-routing algorithms for geomorphic applications, *Geomorphology*, *122*, 91–98.

Pelletier, J. D. (2013), A robust two-parameter method for drainage network extraction from high-resolution DEMs: Evaluation using synthetic and real-world DEMs, *Water Resour. Res.*, doi:10.1029/2012WR012452.

Pelletier, J. D., and C. Rasmussen (2009a), Quantifying the climatic and tectonic controls on hillslope steepness and erosion rate, *Lithosphere*, *1*, 73–80.

Pelletier, J. D., and C. Rasmussen (2009b), Geomorphically-based predictive mapping of soil thickness in upland watersheds, *Water Resour. Res.*, *45*, W09417, doi:10.1029/2008WR007319.

Pelletier, J. D. et al. (2011), Calibration and testing of upland hillslope evolution models in a dated landscape: Banco Bonito, New Mexico, *J. Geophys. Res.*, *116*, F04004, doi:10.1029/2011JF001976.

Perron, J. T. (2011), Numerical methods for nonlinear hillslope transport laws, *J. Geophys. Res.*, *116*, F02021, doi:10.1029/2010JF001801.

Perron, J. T., W. E. Dietrich, and J. W. Kirchner (2008), Controls on the spacing of first-order valleys, *J. Geophys. Res.*, *113*, F04016, doi:10.1029/2007JF000977.

Rasmussen, C. (2008), Mass balance of carbon cycling and mineral weathering across a semiarid environmental gradient, *Geochim. Cosmochim. Acta*, *72*, A778.

Rasmussen, C., and N. Tabor (2007), Application of a quantitative pedogenic energy model to predict soil development across a range of environmental gradients, *Soil Sci. Soc. Am. J.*, *71*(5), 1719–1729.

Rasmussen, C., R. J. Southard, and W. R. Horwath (2005), Modeling energy inputs to predict pedogenic environments using regional environmental databases, *Soil Sci. Soc. Am. J.*, *69*(4), 1266–1274.

Rasmussen C., P. A. Troch, J. Chorover, P. D. Brooks, J. D. Pelletier, and T. A. Huxman (2011), An open system framework for integrating critical zone structure and function, *Biogeochemistry*, *102*, 15–29.

Riebe, C. S., J. W. Kirchner, and R. C. Finkel (2004), Erosional and climatic effects on long-term chemical weathering rates in granitic landscapes spanning diverse climate regimes, *Earth Plan. Sci. Lett.*, *224*(3–4), 547–562.

Roering, J. J. (2008), How well can hillslope evolution models "explain" topography? Simulating soil transport and production with high-resolution topographic data, *Geol. Soc. Am. Bull.*, *120*, 1248–1262.

Roering, J. J., J. W. Kirchner, and W. E. Dietrich (1999), Evidence for nonlinear, diffusive sediment transport on hillslopes and implications for landscape morphology, *Water Resour. Res.*, *35*(3), 853–870.

Roering, J. J., P. Almond, P. Tonkin, and J. McKean (2004), Constraining climatic controls on hillslope dynamics using a coupled model for the transport of soil and tracers: Application to loess-mantled hillslopes, Charwell River, South Island, New Zealand, *J. Geophys. Res.*, *109*, F01010, doi: 10.1029/2003JF000034.

Spencer, J. E., and S. J. Reynolds (1989), Middle Tertiary tectonics of Arizona and adjacent areas, in Jenney, J.P., and Reynolds, S.J., eds., Geologic Evolution of Arizona, *Ariz. Geolog. Soc. Digest, 17*, pp. 539–573.

Strudley, M. W., A. B. Murray, and P. K. Haff (2006), Regolith-thickness instability and the formation of tors in arid environments, *J. Geophys. Res.*, *111*, F03010, doi:10.1029/2005JF000405.

Tucker, G. E., and R. L. Bras (1998), Hillslope processes, drainage density, and landscape morphology, *Water Resour. Res.*, *34*(10), 2751–2764, doi:10.1029/98WR01474.

Tucker, G. E., F. Catani, A. Rinaldo, and R. L. Bras (2001), Statistical analysis of drainage density from digital terrain data, *Geomorphology*, *36*, 187–202.

Tucker, G. E., L. J. Arnold, R. L. Bras, H. Flores, E. Istanbulluoglu, and P. Sólyom (2006), Headwater channel dynamics in semi-arid rangelands, Colorado high plains, USA, *Geol. Soc. Am. Bull.*, *118*, 959–974.

Van Devender, T. R. (1990), Late Quaternary vegetation and climate of the Sonoran Desert, United States and Mexico, in *Packrat middens: the last 40,000 years of biotic change*, edited by Betancourt, J. L., T. R. Van Devender, and P. S. Martin, pp. 134–165, The University of Arizona Press, Tucson, Arizona.

Walther, S. C., J. J. Roering, P. C. Almond, and M. W. Hughes (2009), Long-term biogenic soil mixing and transport in a hilly, loess-mantled landscape: Blue Mountains of southeastern Washington, *Catena*, *79*, 170–178.

Wilson, L. (1973), Variations in mean annual sediment yield as a function of mean annual precipitation, *Am. J. Sci.*, *273*, 335–349.

Whittaker, R. H., and W. A. Niering (1975), Vegetation of the Santa Catalina Mountains, Arizona. V. Biomass, Production, and Diversity along the Elevation Gradient, *Ecology 56*, 771–790.

Wilkinson, M. T., and G. S. Humphreys (2005), Exploring pedogenesis via nuclide-based soil production rates and OSL-based bioturbation rates, *Aust. J. Soil Res.*, *43*, 767–779.

Yang, X., G. A. Tang, C. C. Xiao and F. D. Deng (2007), Terrain revised model for air temperature in mountainous area based on DEMs: A case study in Yaoxian county, *J. Geogr. Sci.*, *17*, 399–408.

Yetemen, O., E. Istanbulluoglu, and E. R. Vivoni (2010), The implications of geology, soils, and vegetation on landscape morphology: Inferences from semi-arid basins with complex vegetation patterns in Central New Mexico, USA, *Geomorphology*, *116*, 246–263.

Yoo, K., and S. M. Mudd (2008), Toward process-based modeling of geochemical soil formation across diverse landforms: A new mathematical framework, *Geoderma*, *146*, 248–260.